Fiber-Reinforced Ti_3SiC_2 and Ti_2AlC MAX Phase Composites

A Thesis

Submitted to the Faculty

of

Drexel University

by

Charles B. Spencer Jr.

in partial fulfillment of the

requirements for the degree

of

Master of Science in Materials Science and Engineering

June 2010

Dedications

This work is dedicated to the practice of ideals, for having a reason to push ahead and for perseverance.

Acknowledgments

I would like to thank all those who have made this work possible. First I must acknowledge Dr. Michel W. Barsoum; advisor, teacher, but more importantly, my mentor, throughout all of this work. For whom without his guidance, and healthy balance between patience and expectation, my time at Drexel University may have gone for naught. I must thank Dr. Miladin Radovic, of Texas A & M University, who helped start this exploration and who acted as a co-advisor throughout my struggles.

I would like to thank my committee members, Dr. A. Zavaliangos, Dr. U. Wegst, Dr. M. Taheri, and Dr. A. Kontsos. They may never know how truly appreciative of their commitment to my committee I am. With short notice, each one of them graciously offered to serve on my committee.

I want to thank all of my colleagues, past and present, from the MAX phase research group at Drexel University for their help, guidance and most importantly friendship; Dr. A. Zhou, Dr. S. Basu, Dr. A. Sakulich, Dr. S. Amini, Dr. T. Scarbozi, Mr. B. Anasori, Mr. S. Miller, Mr. J. Lloyd, Ms. N. Lane, Mr. M. Shamma, and Mr. A. Moseson. And special thanks to Mr. I. Albayrak, my ‘partner in crime’ when it came to creep testing.

Additionally, I would like to thank Dr. Y. Chung, of Drexel University. His support and presence is immeasurable.

Without the master skills of both Mr. Tom Livingstone [Pennsylvania College of Technology] and Mr. Mark Schiber [Hess Labs, Drexel University], I can safely say that this work would never have been completed. I would like to thank them both for completing the machining necessary to complete the creep testing in this work.

And lastly, but certainly not least, I want to thank Dr. L. Hultman, Dr. P. Eklund, and Dr. J. M. Cordoba of Linköping University, Sweden, for their guidance from thousands of miles away.

This work was funded by the Army Research Office (W911NF-07-1-0628), the Metals Division of the NSF (SGER 0736218) and the Swedish Foundation for Strategic Research (SSF).

Table of Contents

LIST OF TABLES

LIST OF FIGURES

ABSTRACT
Fiber-Reinforced Ti_3SiC_2 and Ti_2AlC MAX Phases Composites
Charles B. Spencer Jr.
Dr. Michel W. Barsoum

It was proposed that reinforcing commercially available MAX phase powders would enhance their high temperature mechanical properties in general, and their creep resistance in particular. Three reaction pairs were studied; $Ti_2AlC:Al_2O_3$, $Ti_2AlC:SiC$ and $Ti_3SiC_2:TiC:SiC$. Composites were hot-pressed and hot-isostatic pressed to temperatures as high as 1500 °C. At 1300 °C dense Ti_2AlC-alumina composites were fabricated wherein the fibers did not appear to sinter together. At 1500 °C, the alumina fibers agglomerated and sintered together and presumably lost their structural integrity. At these same temperatures, the SiC fibers reacted with the Ti_2AlC matrix, losing their integrity as well. It was also shown, through the use of differential scanning calorimetry and x-ray diffraction that Ti_2AlC is only kinetically stable at 1500 °C and when the activity of Al in the processing environment is small, Al is lost while Ti_3AlC_2 and Ti-aluminides are formed.

With the $Ti_3SiC_2:TiC:SiC$ combination, however, processed at 1500 °C, no evidence for a reaction was found. The SiC/Ti_3SiC_2 interface remained sharp and reaction free. These samples were fully dense. Preliminary results have shown that ≈ 6 vol. % SiC fibers, decreased the creep tensile strain rates at 1100 °C, and increased the times to failure. Based on this work, we conclude that when continuous SiC fibers are incorporated in Ti_3SiC_2, an increase in the latter's high temperature creep response will occur and is thus a viable method of extending the life of Ti_3SiC_2-based materials in high temperature load bearing applications.

CHAPTER 1. BACKGROUND AND LITERATURE SURVEY

Note: The content of this section has been adapted from two papers for which Charles Spencer was a primary author.[1-2]

1.1 Background on Ceramic-Ceramic Composites

The field of high-temperature, low-density composite materials has been rapidly growing for some time. With great aptitude for applications in the aerospace and sporting goods markets, composites are being developed that replace their monolithic, metallic counterparts.

Composites are made up of two parts, the matrix and the reinforcement. This introduction focuses on ceramic matrices and reinforcements in the form of fibers. In general the function of the matrix is to; keep the fibers in place, help to distribute and transfer the load, protect the fibers in both the structure and during the processing, control the electrical and chemical properties of the finished material, and to carry interlaminar shearing.[3] The functions of the fiber reinforcement are to increase the stiffness and to increase the thermal and electrical conductivity (e.g. rebar in concretes).[3] Aligning the fibers in the matrix can achieve an increase in strength of a specific mode.[3] In a polymer or metal-based composite, the reinforcements are meant to carry the bulk of the applied load and directly increase the strength and stiffness of the material. However, in the case where the matrix is a ceramic material, the reinforcements are used in a different manner. The fibers, of a specific orientation, increase the strength, indirectly by increasing the toughness of the matrix.[3]

i. Material Selection

In the realm of fiber-reinforced ceramic matrix composites, there are three categories of fibers to choose from; whiskers, textile fibers and monofilaments[3]. Whiskers are of the size, roughly 1 μm in diameter and 200 μm in length. They are near single crystals that have strength properties of almost theoretical magnitudes[3]. Although whiskers can enhance the mechanical properties of ceramic matrices, only through continuous fiber reinforcement can reliable, bulk structures be produced[3].

Next in size are the ceramic textile fiber reinforcements. Fibers of this type are made up of variations of three systems; Al_2O_3, Si-C and Si-N. These are used for their high temperature properties and their ability to be shaped into complex pre-forms. These fibers are defined by ρ_{cr}, their critical bend radius, which is the smallest radius that the fibers can bend before they fracture.[3] It can be shown that ρ_{cr} can be calculated by multiplying the failure strain of the fiber by the radius of the fiber. To achieve the most robust fibers, high strengths and low elastic moduli are coupled with fine diameters. The DuPont Company was the first to manufacture these types of fibers, producing DuPont FP, a greater than 99% pure alpha-Al_2O_3 fiber.[3] This material has a reported 2.75 mm critical bend radius. With the addition of partially stabilized zirconia, DuPont was able to cut the critical bend radius by one third. DuPont FP 166 was introduced with a composition of 15-25 % ZrO_2, with the balance of Al_2O_3, which has a ρ_{cr} of 1.83 mm. Further, silica modified alumina has cut ρ_{cr} to 0.5 mm.[3]

Monofilament reinforcements come in two types, boron carbide and silicon carbide. These fibers are produced by chemical vapor deposition, CVD, onto a fine filament substrate. The advantage of the use of these fibers, over textiles and whiskers, are their ability to withstand some degree of surface reaction with the matrix during fabrication. These fibers, because of their large critical bend radius, are limited to pre-forms such as sheets, plates and large diameter cylinders. The matrix material can then infiltrate the fibers by several processing techniques such as, powder sintering, powder hot pressing, plasma spraying and melt infiltration.[3]

The matrix materials for these fiber-reinforced ceramic composites are chosen based on their thermal stability and processing conditions. Most composites are made with oxides, carbides, nitrides, borides and silicides. What ultimately defines what composite can be made is the chemical and mechanical compatibility between the matrix and the fiber. Furthermore, large differences in thermal expansion between the reinforcement and the matrix can result in residual stresses during fabrication, which can lead to degradation of the final mechanical properties.

ii. Processing

The processing of ceramic composites can be carried out using the matrix in one of three phases; solid, liquid or vapor. The goal of these processes is to achieve an even dispersion of the matrix around the fibers. This should create a final product that is of minimum porosity, uniform dispersion of constituents, and a controlled bonding between the matrix and the reinforcing fibers.

a. Powder Processing

The steps included in processing ceramic composites from powdered constituents are as follows; powder selection, powder characterization, agglomerate reduction, mixing, green body fabrication, green body machining, binder removal, densification, burr removal and inspection.[3]

The ceramic powder is selected based on chemical, mechanical and thermoelastic compatibility between the powder and fibers. Also the desired physical and mechanical properties of the resulting product can help define the starting material. Reactions between the fibers and matrix, and also differences in melting temperatures and thermal expansion coefficients, can eliminate certain matrix/fiber combinations.

To reduce voids and increase interfacial strength and the toughening effect of the reinforcing phase, uniformity must be achieved in the mixture. This uniformity is achieved through 'packing' of the matrix powder and the reinforcement fibers. In the case of round fibers, or whiskers, if they are perfectly aligned in a closed packed array then the matrix particles, that are ≈ 0.15 times the size of the fiber diameter, sit in the interstitial positions between the fibers.[3]

Powder can be made up of both primary particles and agglomerates, where agglomerates are a group of primary particles bonded by surface chemical forces, electrostatic forces or solid bridging. In order to have a homogeneous mixture of fibers and powder, these agglomerates must be reduced. If the fibers being used are robust, or if some damage can

be tolerated, then the agglomerates can be broken down mechanically as the constituents are mixed during ball milling.[3]

An organic binder is usually added to the fiber/matrix mixture. This binder ensures that the first consolidation step yields a body that is dense. This consolidated body is referred to as a green body, and usually can be machined without damage. Several processes that can achieve a green body are; uniaxial pressing (CP), cold isostatic pressing (CIP), tape casting, extrusion, compression molding and injection molding.[3]

Final densification can be accomplished at high temperatures, most commonly through sintering, hot pressing (HP) or hot isostatic pressing (HIP). Sintering may be used when attempting composites with a low percentage of fiber (< 5%).[3] However, complete densification during sintering usually involves excessive temperatures and many hours, which may be impractical. In composites with high percentage fiber, HPing and HIPing are the only effective methods to achieve densification. Below can be found Table 1, from the text *Handbook of Composites*, which shows how fiber volume percent affects the densification temperature of SiC-whisker reinforced Al_2O_3 composites. With higher percent fibers, the temperature increases to achieve the same densification as the pure alumina.

Table 1: Effect of processing parameters on the theoretical densities of SiC whisker-Al_2O_3 composites pressed at 31 MPa pressure.[4]

Vol. % Whiskers	Pressing Temperature (°C)	Pressing Time (min)	Density (g cm^{-3})	Density (theoretical)
0	1500	60	3.95	99.1
10	1500	35	3.78	96.7
10	1650	60	3.89	99.5
20	1500	120	3.68	96.1
20	1650	60	3.72	97.1
20	1725	60	3.78	98.6
20	1800	25	3.81	99.5

b. Liquid Processing

The need for high temperatures and large loads to achieve fully dense ceramic composites can adversely impact the final strengths supplied by the fiber reinforcements. By reducing the processing temperature, time and load, the damage to the reinforcements can be minimized. One way to reduce the mechanical damage is to process by infiltration with molten matrices. However, because the high melting temperatures of most ceramics, the general use of this process is limited. With special treatment of the matrix and the use of innovative *in situ* reaction techniques, melt infiltration has been utilized successfully to fabricate ceramic composites.[3]

The literature has stated that as recently as 1998, melt gas-metal reactions have been applied to produce ceramic-matrix composites directly from liquid metals[3]. This process has been commercially developed and is known as the DIMOX™ process of the Lanxide Corporation. During this process oxidation or nitridation forms on the surface of the molten metal, which forms a layer of solid ceramic. The layer then thickens as the molten

metal wicks up between the grains of the ceramic, this process is presented in the Fig. 1.[3]

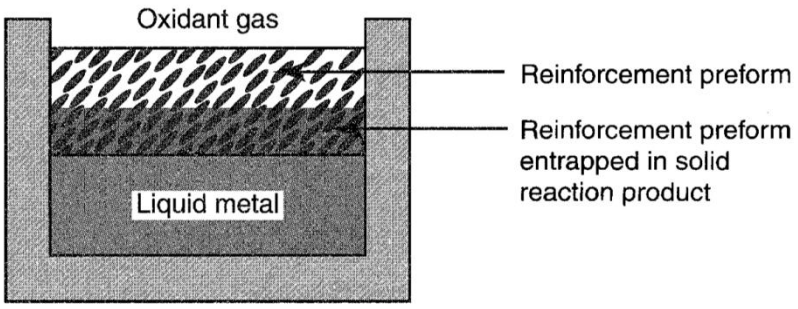

Figure 1: Directional metal oxidation method for processing ceramic composites.[5]

The growth of the ceramic phase is possible by modification of the surface energies between the various phases. In the case where the grain boundary energy, γ_B, is less than twice the energy of the solid-liquid interface, γ_{SL}, and the energy of the solid-liquid interface, γ_{SL}, is greater than the energy of the solid-vapor interface, γ_{SV}, thickening of the reaction compound (oxide, nitride, etc.) layer cannot take place. But by reversing the relative values of the surface energies, the unstable grain boundary will permit wicking of the liquid metal through the grain boundaries of the reaction product phase.[3] A schematic, taken from the *Handbook of Composites*, of this can be in Fig. 2.

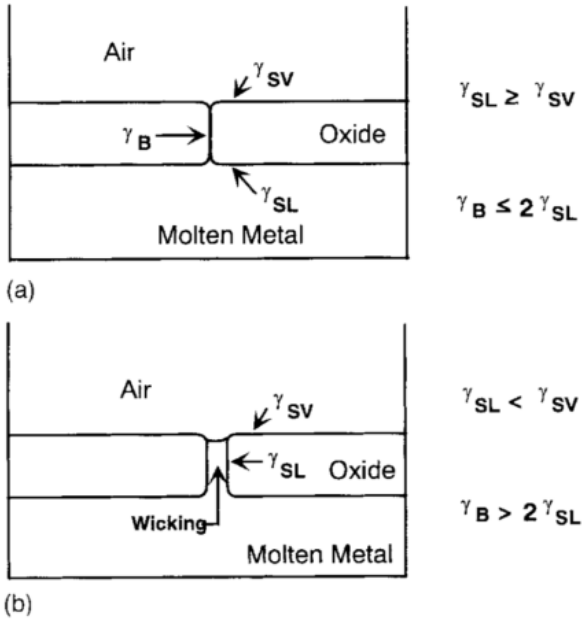

Figure 2[3]: Mechanism of directed metal oxidation growth[6]. (a) no growth due to stable grain boundary; (b) oxide growth mechanism with unstable grain boundary.[3]

c. Vapor Processing

Chemical vapor infiltration, CVI, is the infiltration of the reinforcing phase by a gas that decomposes to form a solid matrix phase[3]. Using this method, various carbides, nitrides, oxides and borides have been deposited on silicon carbide-based yarn fibers like those produced by Nicalon and Tyranno and oxide based fibers like Nextel[3]. Also, deposition has been used with carbon yarn fibers and SiC whiskers. The most common matrix used with this method is SiC.[3]

There are two basic methods of CVI: isothermal processing and forced flow/thermal gradient processing. Isothermal processing heats the fiber pre-form by radiation from the

walls of a furnace or by inductively heating a carbon mandrel on which the pre-form is placed.[3] In either case, the decomposing gases are allowed to diffuse through the fiber pre-form. The forced flow/thermal gradient method takes the reactant gases and forces them through the fiber pre-form, which is retained in a graphite holder with a sharp thermal gradient maintained by water cooling. Below, Fig. 3, is a schematic from the *Handbook of Composites* of the forced flow/thermal gradient method.

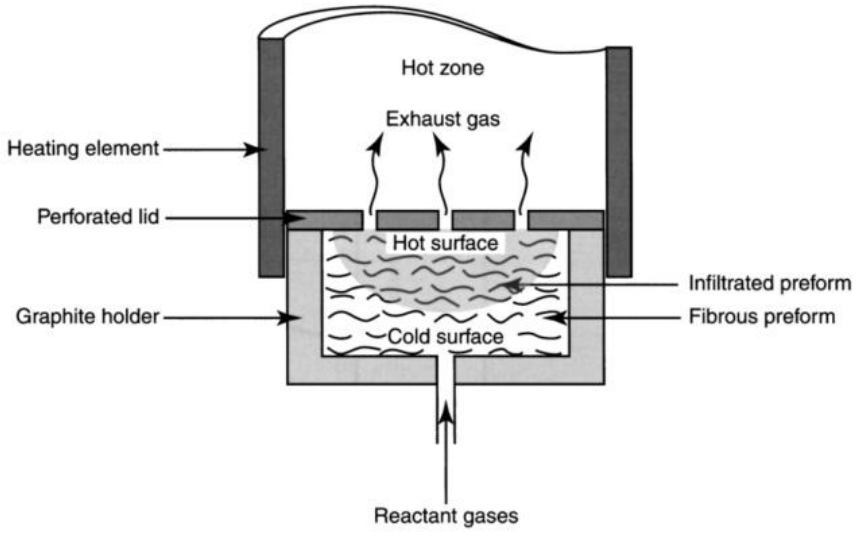

Figure 3[3]: Forced flow thermal gradient method for CVI processing.[7]

Drawbacks to the CVI method include both high processing time and high cost. It is also difficult to achieve 100 % density because as the deposition occurs, pathways begin to block up for the gas to travel. It is necessary to stop the infiltration process to grind the surfaces in order to reopen the pathways to the fibers. A residual porosity of 10-20% and an open porosity of less than 10% are usually obtained with this method.[3]

iii. Design Considerations

As stated above, the rationale for ceramic-based composites is to impart the toughness that is otherwise unachievable with a monolithic ceramic.[3] In designing a fiber-reinforced ceramic composite there are three ways of aligning the fiber reinforcements; continuous unidirectional, discontinuous and multi-directional/multi-layer.

The design considerations are unique for each of these composites. For continuous unidirectional aligned fibers the rule of mixtures can be applied when calculating the resulting elastic and thermoelastic properties of the final product.[3] The Young's modulus of the composite, E_c, is calculated assuming;

$$E_c = V_f E_f + V_m E_m$$

where E_f is the modulus of the fibers, E_m is the modulus of the matrix, V_f is the volume fraction of fibers and V_m is the volume fraction of the matrix. In the composite,

$V_f + V_m = 1$, therefore:

$$E_c = V_f E_f + E_m(1-V_f) \qquad (1.1)^{[3]}$$

However, strength properties cannot be accurately predicted because reinforcement-matrix bond strength and flaw sensitivity are not considered in the rule of mixtures. When the bond strength between the fibers and matrix is at a maximum the strength depends on the relative fracture strains, strength and stiffness of the constituents. There are two combinations that can be made with fibers and matrix. The first is high stiffness, high strength fiber and a lower stiffness, low strain to failure matrix. This strength prediction can be found below, Fig. 4[3];

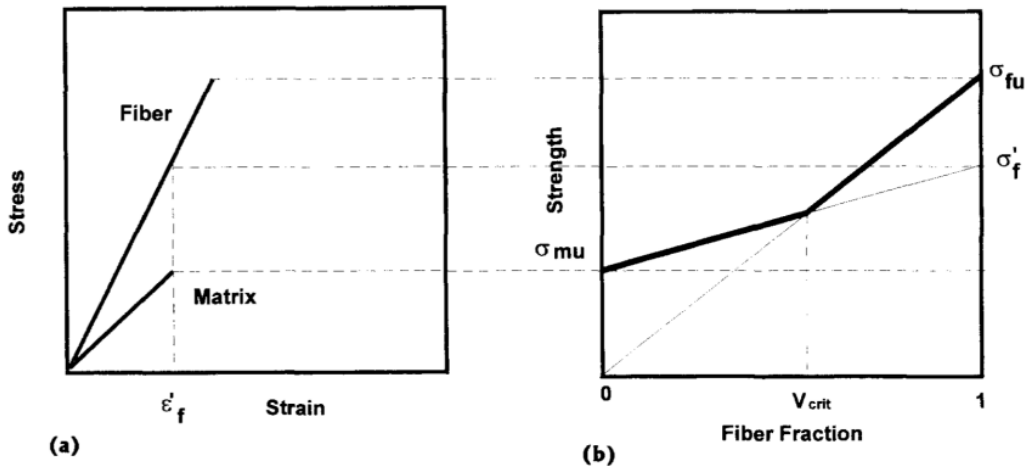

Figure 4[3]: Strength prediction for high stiffness, high strength fiber and a lower stiffness to failure matrix.

At a fiber volume fraction, V_{crit}, the composite fails when the matrix fails. At values below this point there is a simple linear stress-strain behavior to failure, but values above V_{crit} the fibers strengthen the composite. Although the matrix fails before the fibers, the fibers can retain the broken matrix in place before the fibers break at a higher load.[3] In the case where high strength fibers are combined with a higher stiffness, low strain to failure matrix, the predicted strength will decrease with increasing fiber percentage. This is until the $V_f = V_{min}$, where V_{min} is a minimum fiber percentage. Below V_{min} the failure of the matrix still means failure of the composite, and values above V_{min} extend the strength of the matrix with the fiber strength. This can be seen in the charts below, Fig. 5, from the text *Handbook of Composites*.

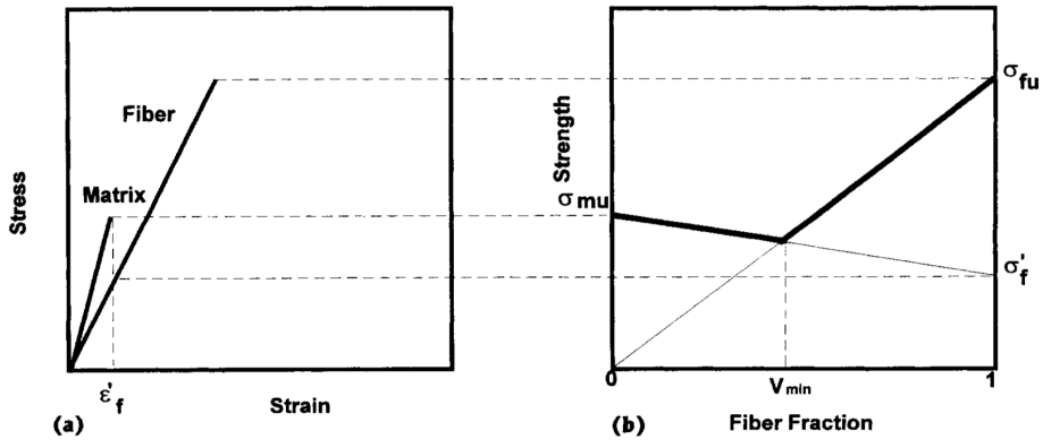

Figure 5[3]: Strength prediction for a high strength fiber and higher stiffness, low strain to failure matrix.

These two descriptions of continuous unidirectional fiber alignment neglect the effect of fracture surface energy.

When working with discontinuously reinforced composites, the rule of mixtures is less important. Here, the goal is to improve the toughness by a combination of fiber pullout, crack deflection and crack bridging. Because the fibers are randomly dispersed the elastic modulus must be broken into the transverse, E_T, and the longitudinal, E_L. These are determined by the Halpin-Tsai relation[3]:

$$E_L = \frac{\left(1+\xi_L \eta_L V_f\right)}{\left(1-\eta_L V_f\right)}$$

$$E_T = \frac{\left(1+\xi_T \eta_T V_f\right)}{\left(1-\eta_T V_f\right)}$$

where

$$\eta_L = \frac{\left(E_f / E_m - 1\right)}{\left(E_f / E_m + \xi_L\right)}$$

$$\eta_T = \frac{\left(E_f / E_m - 1\right)}{\left(E_f / E_m + \xi_T\right)}$$

$$\xi_L = 2\frac{l}{d}, \text{ and } \xi_T = 2$$

Here, V is the volume fraction of the fiber, *f*, and matrix material, m. E is the elastic modulus of the subscripts; m for matrix, *f* for fiber, T for transverse and L for longitudinal.[3] ξ is a measure of fiber reinforcement of the composite material that depends on the fiber geometry, packing geometry and loading conditions[8]. The T and L subscripts stand for transverse and longitudinal.

With the above mathematics, the coefficients of thermal expansion, α_T and α_L, can also be estimated.

$$\alpha_L = \frac{\left(\alpha_f E_f V_f + \alpha_m E_m V_m\right)}{E_L}$$

$$\alpha_T = (1 + \nu_f)\, \alpha_f V_f + (1 + \nu_m)\, \alpha_m V_m - \alpha_L \nu_{LT}$$

where

$$\nu_{LT} = \nu_f V_{f+} \nu_m V_m$$

Here ν_f and ν_m are the Poisson's ratio for the fiber and matrix, respectively.

The elastic modulus of the randomly dispersed fiber composite, E_r, is then calculated from the E_T and E_L:

$$E_r = (3/8)\, E_L + (5/8)\, E_T$$

It is important to point out that all of the calculations pertaining to discontinuous randomly dispersed fiber reinforced composites are for an ideal scenario. They overestimate the value of these properties because of the ineffective bonding between the fiber reinforcement and the matrix and deviation from ideal fiber alignment.[3]

For the design of multilayer/multidirectional reinforcement laminates, both mechanical and physical properties can be predicted from theoretical and semi-empirical treatment of the constituent properties such as; elastic modulus of the fiber and matrix, orientation factor, f, the volume fraction of the fiber, V_f, the fiber aspect ratio, l/d, and the coefficients of thermal expansion of both the fibers and matrix material.[3] Using the classical laminate plate theory, the elastic and thermoelastic properties can be predicted from the layer properties.[3] However, the strength cannot be predicted this way because of unknown flaws in the resulting composite. For this, modified laminate fracture theories must be employed.[3]

In any of the fiber orientations from above, the design must also keep in mind symmetry and balance. In composites, this refers to the geometric mid-plane that acts as a reference surface for determining if a laminate is symmetrical. In order to reduce out-of-plane strains, coupled bending and stretching of the laminate, and complexity of analysis, symmetric laminates should be used.[3] Balance helps the laminates achieve in-plane orthotropic behavior. Balance is achieved by ensuring that for every layer of fibers, there

is another layer of opposite orientation. Laminates that only contain 0° and/or 90° layers satisfy the requirements for balance.[3]

iv. Failure Modes

Failure modes for unidirectional continuous, monofilament fiber-reinforced ceramic composites are mode I, mode II and mixed mode I/II[9]. In tensile loading, mode I is the main factor with contributions from debonding and sliding. Matrix cracking results first, then failure of the fibers follows. If the interfacial bonding between the fibers and matrix is weak, pullouts may occur. Mode II is the failure mechanism under shear loading, with damage occurring at quite low shear stresses. This mode of failure is governed by microcracking, which are presumably caused by stress concentrations in the matrix that form normal to the local principal tensile stress, but then deflect to the mode II plane and combine. The two modes are linked as it has been shown that as the shear strength decreases, the mode I toughness increases. The mixed mode conditions can exploit failure along the fiber-matrix interface. Because this interface can have a lower fracture resistance than either the fibers or the matrix, the debond crack can continue to extend along the interface.[9]

1.2 Properties of MAX Phases and MAX Phase Composites

MAX phases, named for their general formula of $M_{n+1}AX_n$ (n=1,2,3), are a group of nanolayered ternary carbides and nitrides where *M* is an early transition metal, *A* is an A-group (mostly IIIA and IVA) element, and *X* is either a C and/or N[10-13]. These phases have a hexagonal crystal structure with the space group $P6_3/mmc$, having two formula

units per unit cell. They consist of $M_{n+1}X_n$ layers that are interleaved with pure A-group layers.[14] To date, there are over 60 known MAX phases. Subsequently, these phases come in three variations. The largest group of these phases, where roughly 50 combinations exist, is the form M_2AX[15], which includes Ti_2AlC, V_2GaN and Ti_2SC. There are five of the form M_3AX_2[16-20], which includes such materials as Ti_3SiC_2 and Ti_3AlC_2. With the form of M_4AX_3 rounding off the last seven[18, 21-27]. Examples of this 413 phase are Ta_4AlC_3 and Ti_4AlN_3.[14, 28] A comprehensive listing of these phases can be found below as Table 2.

Table 2: Summary of MAX phases known to date.

211	Ti_2AlC	Ti_2AlN	Hf_2PbC	Cr_2GaC	V_2AsC	Ti_2InN
	Nb_2AlC	$(Nb,Ti)_2AlC$	$Ti_2AlN_{0.5}C_{0.5}$	Nb_2GaC	Nb_2AsC	Zr_2InN
	Ti_2GeC	Cr_2AlC	Zr_2SC	Mo_2GaC	Ti_2CdC	Hf_2InN
	Zr_2SnC	Ta_2AlC	Ti_2SC	Ta_2GaC	Sc_2InC	Hf_2SnN
	Hf_2SnC	V_2AlC	Nb_2SC	Ti_2GaN	Ti_2InC	Ti_2TiC
	Ti_2SnC	V_2PC	Hf_2SC	Cr_2GaN	Zr_2InC	Zr_2TiC
	Nb_2SnC	Nb_2PC	Ti_2GaC	V_2GaN	Nb_2InC	Hf_2TiC
	Zr_2PbC	Ti_2PbC	V_2GeC	V_2GeC	Hf_2InC	Zr_2TiN
312	Ti_3AlC_2	Ti_3GeC_2				
	Ti_3SiC_2	Ta_3AlC_2				
	Ti_3SnC_2					
413	Ti_4AlN_3	Ta_4AlC_3	Ta_4AlN_3			
	Ti_4SiC_3	Nb_4AlC_3				
	Ti_4GeC_3	V_4AlC_3				

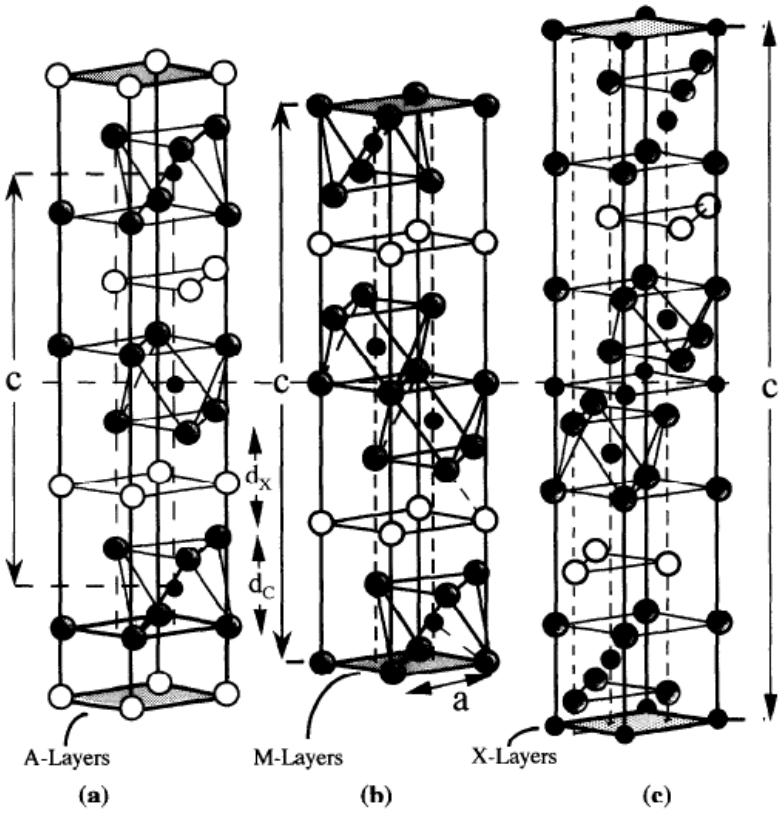

Figure 6: MAX unit cells of; (a) 211, (b) 312 and (c) 413. Vertical arrows labeled c, denote the unit cell, while a horizontal line marks the center of each unit cell.[29]

These extraordinary ternary carbides were first discovered as early as the 1960's when Nowotny and his colleagues reported approximately 30 phases, then referred to as H-phases[13, 15, 29]. H-phases are of the form M_2AX (Fig. 6a) and included the phases Ti_2AlC and Ti_2AlN.[13, 29] The phase Ti_3SiC_2 was then discovered by Nowotny et al. in 1967, which is structurally related to the 211 phases, where M_3C_2 layers are interleaved with pure *A*-layers[30]. (Fig. 6b)

The MAX phases combine properties that are a mixture of metallic and ceramic materials. Similar to their corresponding binary carbides and nitrides, they are elastically stiff, have relatively low thermal expansion coefficients and are resistant to chemical attack. These phases, however, could not be more different than their binary cousins when it comes to their mechanical response. They are relatively soft (1-5 GPa) and machinable, thermal shock resistant, damage tolerant, and have good thermal and electrical conductivities. Some are even fatigue, creep and oxidation resistant.[14]

1.2.1 Ti_2AlC

Ti_2AlC, which crystallizes in the Cr_2AlC-type structure (Fig. 6a) is of particular interest. The atoms are located at the following Wycoff positions: Ti at 4*f*, Al at 2*c* and C at 2*a*, with the lattice constants being a=3.04 Å and c=13.60 Å.[31] The hardness and room temperature electrical and thermal conductivities were reported by Barsoum et al. to be 4.5-5.5 GPa, $2.7x10^6$ -$2.8x10^6$ Sm[32-33] and 33-46 Wm/K, respectively.[33-34] It's Poisson's ratio, Young's, shear and bulk moduli are 0.19, 277 GPa, 118 GPa and 186 GPa, respectively[35-36].

In addition, the room temperature compressive strength of Ti_2AlC fabricated by a reactive hot-isostatic pressing method at 1600 °C was reported to be 540 MPa. When the material was taken to T ≈ 1000 °C the deformation became plastic and strongly depended on the strain rate. The yield point was in the range of 270-435 MPa between 1000°C and 1300°C.[33, 37] Wang et al. recently reported on the room temperature compressive and

flexural strengths as 670 and 384 MPa, respectively, a fracture toughness of 7.0 MPa-$m^{1/2}$ and Vickers hardness values between 4.2-5.7 GPa for hot pressed Ti_2AlC.[38]

The attractiveness of Ti_2AlC for high temperature applications, however, derives mostly from its superb oxidation resistance.[39-40] Early work on the oxidation behavior of Ti_2AlC,[41-42] showed that oxidation occurred by the inward diffusion of oxygen and the outward diffusion of Al^{3+} and Ti^{4+} ions through a $(Ti_{1-y}Al_y)O_{2-y/2}$ oxide surface layer and that the oxidation kinetics were parabolic up to 1100 °C at short times (up to 20 h). Wang and Zhou reported that Ti_2AlC follows a cubic oxidation law in the 1000-1300°C range, where scale growth is governed by oxygen grain-boundary transport.[40] The scales reported by Wang and Zhou were fully dense, adherent and resistant to thermal cycling.[40] More recently, Sundberg et al. showed that dense, crack-free, stable and protective alumina, Al_2O_3, scales form on Ti_2AlC surfaces. These scales did not spall off even after 8,000 thermal cycles to 1350 °C.[39] The remarkable thermal shock resistance of the protective oxide scale was attributed to the fact that the thermal expansion coefficient of Ti_2AlC ($8.2x10^{-6}$ K^{-1})[33] and Al_2O_3 are quite similar. Lastly, Byeon et al.[43] confirmed that the compressive residual stresses formed during oxidation of Ti_2AlC are small. They also demonstrated that the oxidation and spallation resistance of Ti_2AlC is comparable, and sometimes even better than those of the best-known alumina-forming materials currently available. These adherent scales make Ti_2AlC a strong candidate for high temperature structural applications.

Despite the potential for Ti_2AlC to be used as a high temperature structural material, surprisingly no results on its creep behavior have been published to date.

1.2.2 Ti_3SiC_2

Although Ti_3SiC_2 was first discovered in 1967 by Jeitschko and Nowotny[30] through a reaction between TiH_2, Si and graphite at 2000 °C , it was not until a few decades later, in 1996, that Barsoum and El-Raghy[44] could synthesize a bulk sample of full density and purity through reactive hot pressing Ti, graphite and SiC powders at 1600 °C. This is not to say there were not many attempts at synthesis and characterization. Many works have been completed to synthesize Ti_3SiC_2. After the work of Jeitschko and Nowotny came the work of Nickl et al. in 1972, where they used $TiCl_4(g) + SiCl_4(g) + CCl_4(g) + H_2(ex)$ to deposit a thin film of Ti_3SiC_2 and $Ti_5Si_3C_x$[31, 45]. Racault et al. additionally published on reactive sintering of Ti_3SiC_2; however, they were unable to achieve single-phase.[46] Over the years from 1967 to present, many techniques had been employed to synthesize this phase, but most had either failed to be replicable in bulk or unable to produce pure, single phase. These methods include; magnetron sputtering (MS)[25, 47-48], pulsed laser deposition (PLD)[49], self-propagating high-temperature synthesis (SHS)[50-51], arc-melting and post annealing[52], spark plasma sintering (SPS) and pulse discharge sintering (PDS)[53-55], pressureless sintering[56-57], and mechanical alloying (MA)[58-61].

The mechanical response of Ti_3SiC_2 has been extensively studied and reported for both fine grained (FG), 3-5 μm, and coarse grained (CG), 100-200 μm, microstructures. At room temperature, Ti_3SiC_2 exhibits brittle failure with compressive strengths reported as

1050 and 720 MPa and flexural strengths of 600 and 330 MPa, for CG and FG, respectively. It has been shown that with increasing the temperature the compressive strength decreases and at T > 1200 °C, both microstructures exhibit plastic deformation, with yield points of 500 MPa and 320 MPa for CG and FG, respectively. At T = 1300 °C the flexural strengths were reported to drop to 120 and 100 MPa, respectively.[62] In addition, Ti_3SiC_2 is damage tolerant and thermal shock resistant. The CG microstructure is thermal shock resistant up to 1400 °C, while the FG microstructure loses strength gradually when quenched from 750 °C and 1000 °C by 10 % and 50 %, respectively.[62]

The oxidation kinetics and morphology of the oxide phases that form on Ti_3SiC_2 at temperatures up to 1300 °C have been studied intensively over the last decade[61]. Barsoum et al.[63] showed that long term oxidation (up to 1500 h) of Ti_3SiC_2 resulted in the formation of a TiO_2 outer scale and mixed TiO_2 and SiO_2 inner scale due to the inward diffusion of oxygen and outward diffusion of Ti and C. They also showed that oxidation kinetics at temperatures of 1000 °C or greater and times greater than 30 h changes from parabolic to linear. Sun et al.[64] and Liu et al.[65] investigated the cyclic-oxidation behavior of Ti_3SiC_2 in air at 1100 °C and showed no spallation or separation of oxide scales up to 360 cycles despite the formation of a large number of microcracks in the oxide scale. The latter contributed to the faster oxidation kinetics when compared to the isothermal oxidation.

Radovic et al. and Zhen et al. studied creep extensively in both coarse- and fine-grained Ti_3SiC_2 materials. In the coarse-grained material (>20 μm) the dominating mechanism

for creep is through dislocation creep and high plastic anisotropy in the Ti_3SiC_2 results in large internal stresses.[66-67] Dislocation creep is defined as;

$$\dot{\varepsilon} = \boldsymbol{b}\left\{\rho\upsilon(\sigma) + \frac{d\rho(\sigma)\lambda}{dt}\right\} \qquad (1.2)^{[68]}$$

where $\boldsymbol{b}$ is the Burger's vector, ρ the dislocation density, $\upsilon(\sigma)$ the average velocity of a dislocation at an applied stress σ, $d\rho/dt$ is the rate of nucleation of the dislocations at stress σ, and λ is the average distance they move before they are pinned[68]. Also, the brittle-to-plastic, BTD, transition was found to be between 1100-1200°C. At this transition the fracture toughness of Ti_3SiC_2 drops from about 8-10 MPa $m^{-1/2}$ to roughly 4 MPa $m^{-1/2}$. These events lend a hand in high temperature failure of the MAX phase.[66]

1.2.3 MAX Phase Composites

a. Ti-Al-C Reinforced

The reinforcement of Ti_3AlC_2 with 10% by volume Al_2O_3 has been shown by Chen et al. The addition of the α-Al_2O_3 significantly enhanced the strength of the Ti_3AlC_2 in the brittle mode of failure regime, but due to softening of the matrix, strength in the ductile mode of failure had little improvement. It was shown that both the Ti_3AlC_2 and Ti_3AlC_2/10 vol.% Al_2O_3 composite strengths decrease with increasing temperature.[69]

b. Ti-Si-C Reinforced

Benko et al. increased the Young's modulus and Vickers hardness of Ti_3SiC_2 by hot-pressing cubic boron nitride (cBN) with Ti_3SiC_2. The extreme hardness of cBN, which is second only to diamond, drastically improved that of the Ti_3SiC_2 from a Vickers hardness

value of 4 GPa to 19.9 GPa (Vickers hardness for TiC = 16.0-28.0 GPa[68]). The addition of the cBN also increased the modulus from 320 GPa to 525 GPa.[70]

Several composites utilizing Ti_3SiC_2 and a binary carbide have been explored in recent years. Wang et al. [71] used Ti and SiC powders to fabricate nanostructured Ti_5Si_3-TiC-Ti_3SiC_2. Konoplyuk et al. [72-73] used pulsed discharge sintering to synthesize Ti_3SiC_2/TiC composites. Using initial powders of TiH_2/SiC/TiC, samples were sintered with (001) texture and exhibited hardness values of 4-6 GPa and a flexural strength of 400-550 MPa. Ho-Duc et al.[74] studied the fabrication of Ti_3SiC_2/TiC and Ti_3SiC_2/SiC, 30 vol.% reinforcement, composites by hot-isostatic pressing Ti, SiC and C powders for 8 h at temperatures as high as 1600 °C. Flexural strength of both composites decreased, but damage tolerance and thermal shock resistance increased up to a quenching from 1400°C.

c. MAXmet

Recent studies by several groups have shown the possibilities of reinforcing such MAX phases as Ti_2AlC and Ti_3SiC_2 with metals, such as Ag, Cu and Mg. Ngai et al. and Zhang et al. have reinforced Cu matrices with particulates of Ti_3SiC_2. To enhance the tribological performances of several MAX phases, Gupta et al. reinforced Ta_2AlC and Cr_2AlC with 20% Ag. It is proposed that these composites be used as a high-temperature solid-lubricant that could be used against Ni-based superalloys and alumina.[75] Work presented by Amini et al.[76] has recently shown the successful reinforcement of Ti_2AlC with nano-particles of Mg, a 50/50 mix. The resulting composite was readily machinable,

stiff (≈ 70 GPa), strong, light (2.9 g/cm^3) and exhibited exceptional damping capabilities[76].

If the MAX phases are ever to be used in high temperature, mechanical applications, they will need to be reinforced with ceramic fibers. To the best of our knowledge neither Ti_2AlC nor Ti_3SiC_2, or any of MAX phase for that matter, has ever been reinforced with ceramic fibers. However, from the work of Chen et al. on Ti_3AlC_2/10% by vol. Al_2O_3 and Radovic et al. on creep of MAX phases, it is our belief that if the MAX phases could be reinforced with stiff fibers, the internal stresses occurring due to applied loads at elevated temperatures could be taken up by the fibers. It was our contention that Al_2O_3 or SiC fibers would be a good match for these phases.

1.3 High Temperature Creep Mechanical Testing

It can be said, for a simplistic model, that metals and ceramics will deform at room temperature in a way that depends on stress and is independent of time. However, at elevated temperatures, the material response will not only depend on stress but also temperature and time. This is considered creep and can be defined as the slow, continuous deformation of a material with time at a high temperature. But what is considered a high temperature? Materials have all different values of melting temperatures which range from ice at 0 °C to diamond at 3727 K. It is generally accepted that creep will occur according to the following equations:[77]

$$T > 0.3 \text{ to } 0.4\, T_M \text{for metals}$$

$$T > 0.4 \text{ to } 0.5 T_M \text{for ceramics}$$

It has been well established that creep is manifested in metals by grain boundary sliding and cavity growth. For these reasons, single-crystal superalloys have been developed for the use as turbine blades, which are very creep resistant. However, for the case of ceramics, several different mechanisms can be operative during varying temperatures. Generally, creep in ceramics depends on; stress, strain, time, temperature, grain size and shape, microstructure, etc.[68]

Creep testing can be completed in either compression or tension, with constant load inside a furnace that is maintained at a constant temperature. To analyze the results, strain, ε, is plotted vs. time, T. A typical creep plot is shown in figure 7.

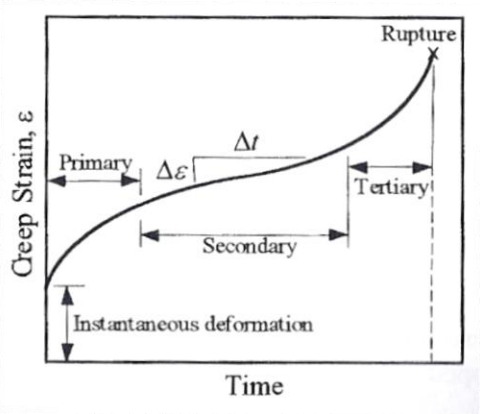

Figure 7: Typical creep strain versus time creep curve showing three regions; primary, secondary and tertiary. Creep strain rates are obtained in the secondary region. Experimentally, not always all three regions are observed.[68]

CHAPTER 2. REACTION STUDIES

Note: The content of this section has been adapted from two papers for which Charles Spencer was a primary author.[1-2]

2.1. Ti_2AlC:Al_2O_3

2.1.1 Synthesis

The Ti_2AlC powder used was a - 325 mesh powder [3ONE2, Voorhees, NJ]. Two types of Al_2O_3 fibers were used: 10 μm diameter [3M Nextel, St. Paul, MN] and ≈ 3 μm diameter [Zircar Ceramics, Florida, NY] fibers. In both cases, the fibers were chopped with a razor blade into ≈ 5 cm lengths. Mixing of the powder and fiber was carried out in several ways: i) *in situ* layering of powder layers, interspersed with layers of chopped fiber; ii) dry mixing by shaking in a plastic bottle; iii) powders and fibers were dispersed in an ethanol solution, mixed with a magnetic stirrer and allowed to dry; iv) dispersed in an ethanol solution and mixed in a plastic bottle placed on a ball mill (without balls), for ≈ 12 h and then allowed to dry.

Table 3: Summary of runs made herein. Column 1 lists the fiber diameter, 211; column 2 the matrix/fiber molar ratio. The key to the label listed in column 7 is: 211 (for Ti_2AlC powder) or fiber diameter or DSC, followed by fiber vol. fraction, followed by consolidation method or DSC and last the processing temperature. The processing time was 3 or 4 h.

Fiber Dia. (μm)	Molar Ratio	Vol. %	Proc. Meth	T (°C)	Time (h)	Label	Major Phases Present
211^	N/A	N/A	HIP	1400	3	211-HP-1400	211
211^	N/A	N/A	HP	1500	4	211-HP-1500	312
3	1.3:1	40	HIP	1300	4	3-40-HIP-1300	211
10	4.1:1	17	HIP	1300	4	10-17-HIP-1300	211
3	7.6:1	9	HIP	1500	4	3-9-HIP-1500	312 + TiC
10	7.6:1	9	HIP	1500	4	10-9-HIP-1500	312
3	1:1	46	HIP	1500	4	3-46-HIP-1500	312
10	1:1	46	HIP	1500	4	10-46-HIP-1500	312 + TiC
10	7.6:1	9	HP	1500	4	10-9-HP-1500	211 + 312
10*	3:1	21	DSC	1410	0	DSC-1410	211+312+TiC
10*	3:1	21	DSC	1550	0	DSC-1550	211 + 312 + TiC

^ Ti_2AlC powder only

* Fibers were manually crushed, mixed with Ti_2AlC powder and cold pressed into small pellets that were then introduced into the DSC.

Prior to HIPing, the mixed dried powders – with various volume fractions of alumina fibers (Table 3, above) - were loaded in a steel die and compressed to loads corresponding to stresses of 57 or 97 MPa for 60 s into 12.5 x 70 mm^2 bars or 25 mm diameter discs, respectively. On an as needed basis, polyvinyl alcohol ≈ 5 ml per 15 grams of powder, was added as a binder to enhance the strength of the green bodies. The latter were then placed in a graphite crucible and covered in a bed of borosilicate glass [Fisher Scientific, Pittsburgh, PA]. The HIP [Flow Autoclave Systems Inc., Columbus, OH] was then sealed and the temperature ramped to 750 °C or 850 °C at 10 °C/min, then subsequently ramped to 850 °C or 1000 °C at 2.5 °C/min and 5 °C/min, respectively. These intermediate temperatures were held for 60 mins, before further pressurizing with

Ar. Once pressurized the temperature was increased again at 10 °C/min up to temperatures of 1300-1500 °C and held at these temperatures for 4 h before furnace cooling. The pressure at temperature was ≈100 MPa.

Three specimens – two pure Ti_2AlC and one containing 9 vol. %, 10 μm chopped in situ layered Al_2O_3 fibers - were hot pressed in a graphite heated hot press [Series 3600, Centorr Vacuum Industries, Somerville, MA] under a vacuum of 10^{-2} torr, and ramped at 500 °C/h to 1400 or 1500 °C and held for 3 or 4 h, in the graphite dies. The load at maximum temperature corresponded to a stress of 20 MPa.

A 3:1 molar ratio of Ti_2AlC powder and 10 μm Al_2O_3 fibers - pre-crushed in a mortar and pestle - were ball milled, using alumina balls, for ≈ 12 h and compacted into green bodies (dia. = 13 mm) with a small pellet press. These pressed pellets were then cut to a size of ≈ 4 mm height by 5 mm dia., and placed in a combined differential scanning calorimetry (DSC) and thermogravimetric unit [Netzsch-STA 449 C Jupiter®], equipped with a mass spectrometer [Netzsch-QMS 403 C Aëolos®] and heated at 20 °C/min up to 1410 °C or 1550 °C in an ultra pure He atmosphere.

2.1.2 Characterization

The HIPed, HPed samples and those placed in the DSC were powdered, using a diamond coated needle file, for x-ray diffraction (XRD) [Model 500D, Siemens, Karlsruhe, Germany and PW1729, Philips, Eindhoven, Netherlands]. In most cases, 10 wt. % pure silicon, Si, powder was used as an internal standard. Scans were made with Cu K_α

radiation (40 kV and 30 mA) at rates of 1.2 or 2.4 deg (2Θ)/min, using steps of 0.02 or 0.04 deg, respectively.

Post DSC, runs were scanned with Cu K_α radiation (40 kV and 40 mA) at 0.057 deg (2Θ)/min. Select runs were scanned from 41–48° 2Θ at rates of 0.12 (2Θ)/min, in order to detect any hints of Al-Ti intermetallics.

Samples were also cut with a precision diamond saw [Struers Accutom-5, Westlake, OH], mounted and polished to a 1 μm diamond suspension. A scanning electron microscope (SEM) [Zeiss Supra 50VP, Thornwood, NY] equipped with energy-dispersive spectroscopy (EDS) [Oxford Inca X-Sight, Oxfordshire, UK] and a microprobe [Cameca SX50, Nampa, ID] equipped with a wavelength-dispersive spectrometer (WDS) [PGT, Princeton, NJ] were used for microstructural and elemental analysis. Select surfaces were then etched with a 1:1:1 ratio of water, concentrated HF and HNO_3 for 5 s and immediately rinsed with water. The microstructure was then viewed under an optical microscope, OM, [Olympus PMG3, Center Valley, PA or KEYENCE VHX 600, Woodcliff Lake, NJ].

2.1.3 Results

a) Monolithic Bulk

Rietveld analysis of the as-received powders (Table 4) indicates that it contains ≈ 14 mol. % Ti_3AlC_2 and ≈ 19 mol. % TiC. Note that these results only quantify the crystalline phases; the presence of amorphous titanium-aluminide intermetallic phases (see below) cannot be ruled out at this juncture.

Table 4: Summary of Rietveld analysis of as-received powders and $3Ti_2AlC + Al_2O_3$ powder mixture after heating twice to 1410 °C or 1550 °C in a DSC at 20 °C/min and immediately cooling at same rate. The goodness of fit, χ^2, is indicated.

Phases	Molar Fraction	Lattice Parameter	
		c (Å)	a = b (Å)
As-received powders			
Ti_2AlC	0.67	13.6946	3.0600
Ti_3AlC_2	0.14	18.540	3.0652
TiC	0.19	a = 4.3093	
1410 °C DSC $\chi^2 = 2.1$			
Ti_2AlC	0.65	13.6711	3.0602
Ti_3AlC_2	0.22	18.5153	3.0709
Al_2O_3	0.13	13.0100	4.7669
1550 °C DSC $\chi^2 = 3.9$			
Ti_2AlC	0.65	13.6143	3.0523
Ti_3AlC_2	0.20	18.4585	3.0685
Al_2O_3	0.14	12.9879	4.7552

When the XRD spectrum of the as-received Ti_2AlC powder (Fig. 8a) is compared to one after HPing the same powders at 1500°C for 4 h (Fig. 8b) it is obvious that Ti_2AlC converts to Ti_3AlC_2. Note that in most XRD spectra, the peak intensities are normalized by the intensity of the internal standard Si peaks and are thus comparable on an absolute scale. A comparison of the two spectra also leaves little doubt that HPing in general reduces the peak intensities.

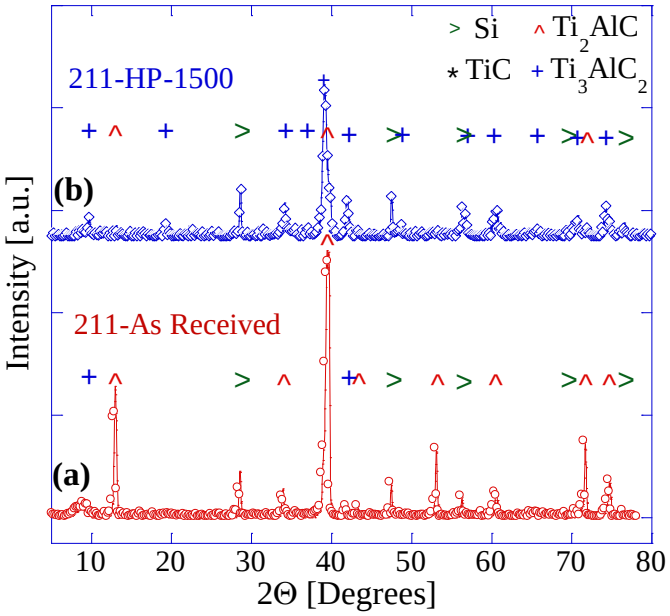

Figure 8: XRD spectrum of, a) as-received Ti_2AlC powder and, b) sample 211-HP-1500. Pure Si was added as an internal standard and all peaks were normalized to the Si peak at 28.44° 2Θ.

A typical backscattered electron SEM micrograph (Fig. 9a) of the same sample – that was fully dense - showed the presence of two phases. The light grey phase, encompassing ≈ 96% of the image area, is identified by EDS (Fig. 9b) to be Ti_3AlC_2, since the Ti:Al ratio is ≈ 3.28±0.1 (e.g. points 1, 4 and 6, Fig. 9b). The darker grey, minority phase - making up the remaining 4% of the imaged area - is an Al-Ti intermetallic (e.g. points 2, 3, 7 and 8, Fig. 9b). At 2.5±0.26, the Al:Ti ratio suggests its chemistry is between $TiAl_2$ and $TiAl_3$. Speckles of a black phase, identified as Al_2O_3, covers less than 1% of the area. In an attempt to find XRD evidence for Ti-Al intermetallics, a slow XRD scan was carried out in the 41-48° 2Θ range of sample 211-HP-1500 (not shown). No peaks belonging to

any Ti-aluminide intermetallics were found, suggesting them to be amorphous or at least nano-crystalline.

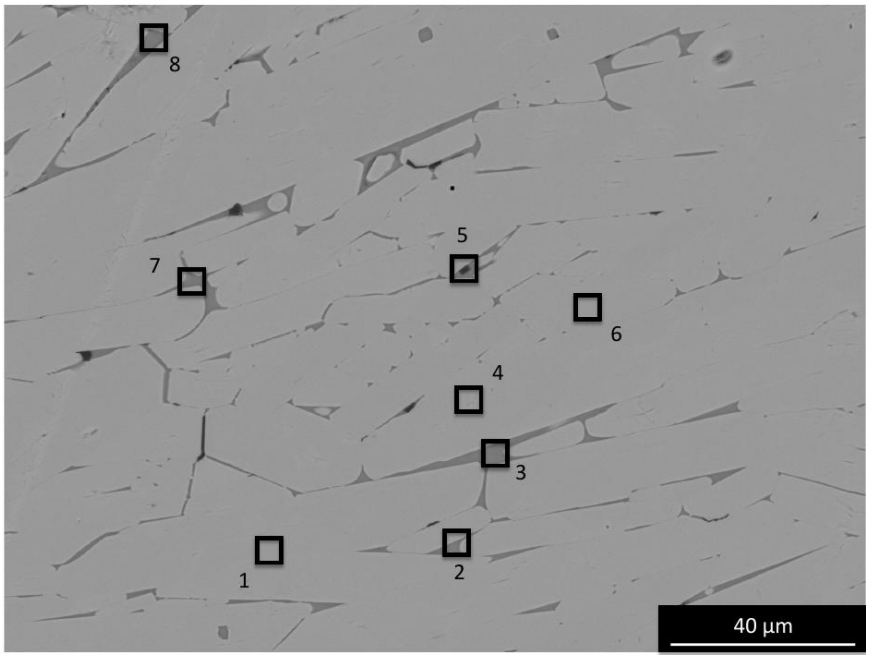

(a)

	Atomic %				
Point	C K	Al K	Ti K	O K	Major Phase
1	29.52	16.39	54.09	--	Ti_3AlC_2
2	11.17	61.87	26.96	--	Al_3Ti
3	9.95	65.46	24.59	--	Al_3Ti
4	29.84	16.42	53.74	--	Ti_3AlC_2
5	4.58	31.75	6.76	56.91	Al_2O_3
6	29.71	16.44	53.85	--	Ti_3AlC_2
7	8.61	62.17	29.22	--	Al_3Ti
8	10.47	64.91	24.62	--	Al_3Ti

(b)

Figure 9: (a) Backscattered electron image of 211-HP-1500. b) EDS results of regions numbered in a. Three phases are present; light grey (Ti_3AlC_2), dark grey (Al_xTi) and black (Al_2O_3).

b) Fiber Composite

When typical XRD diffractograms of HIPed composite samples are compared (Fig. 10) it is obvious that, here again, HIPing results in, i) a diminution of the peak intensities belonging to Ti_2AlC; ii) peak broadening; iii) the emergence of peaks belonging to Ti_3AlC_2 and TiC_x (Figs. 10b, 10c and 10d). The latter are much more pronounced at 1500 °C, than at 1300 °C (compare Fig. 10a to 10b or 10d for e.g.). The transformation of the sample containing 9 vol. % is also less than the one containing 46 vol. % Al_2O_3 fibers.

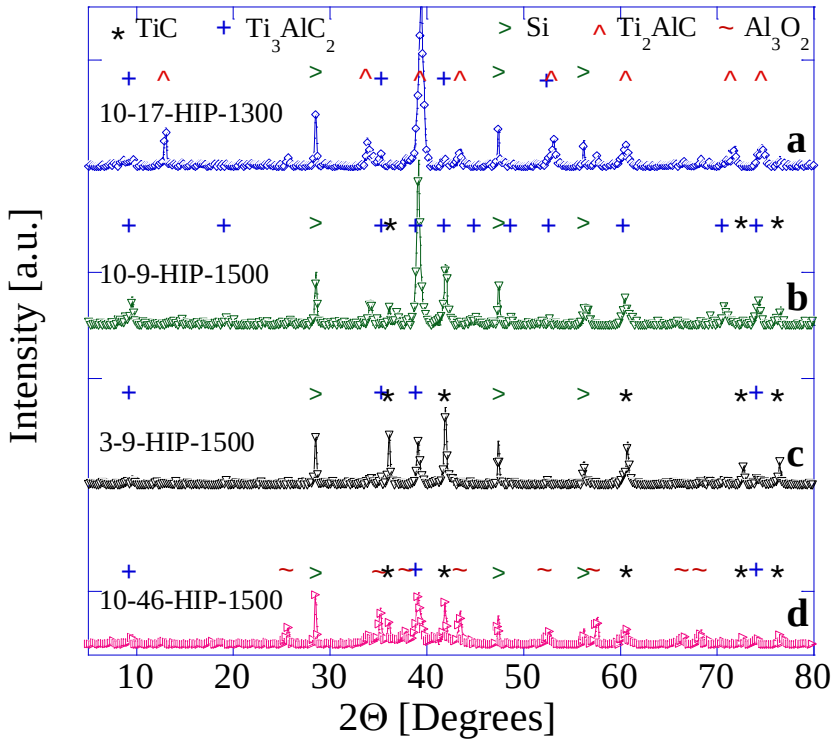

Figure 10: X-ray diffraction patterns of samples, a) 10-17-HIP-1300, b) 10-9-HIP-1500, c) 3-9-HIP-1500 and, d) 10-46-HIP-1500. All spectra normalized to 10 wt. % Si.

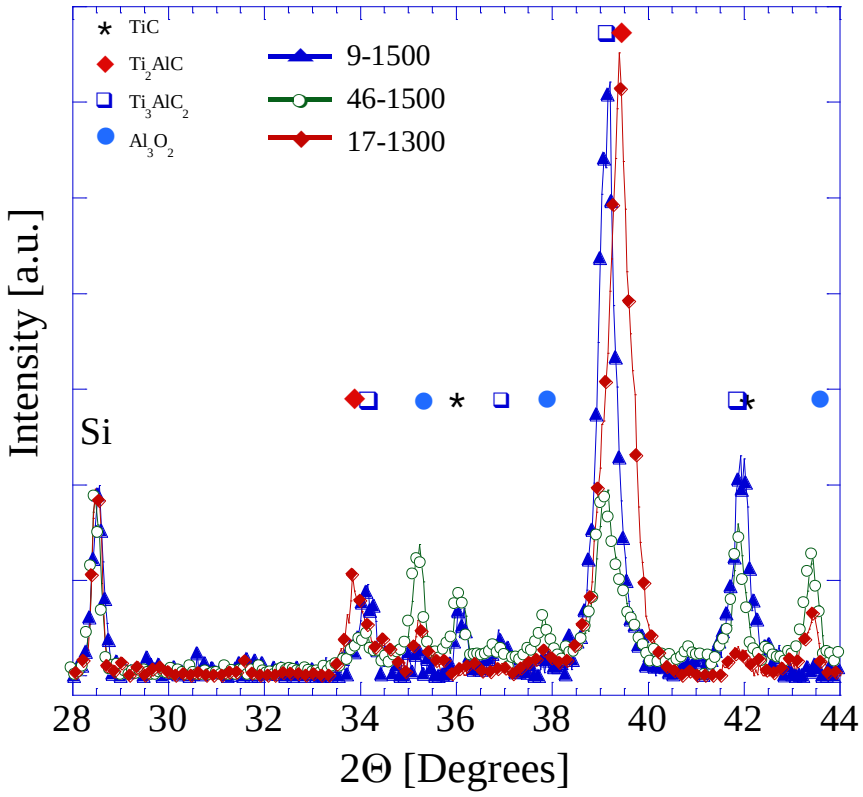

Figure 11: X-ray diffraction spectra from 28 to 44° 2Θ of samples 10-9-HIP-1500, 10-46-HIP-1500 and 10-17-HIP-1300.

Confirmation of these important conclusions can be found in Fig. 11, where slow XRD spectra - from 28 to 44° 2Θ - of samples 10-9-HIP-1500, 10-46-HIP-1500 and 10 17-HIP-1300 are compared. Here again, not only is the 211 phase retained after HIPing at 1300 °C for 4 h (red solid diamonds) but, as importantly, the TiC phase present in the starting powder (Table 4) disappears.

The results of the Rietveld analysis of the $3Ti_2AlC:Al_2O_3$ powder mixture heated twice to 1410 °C in the DSC are listed in Table 4. Only three phases, Ti_2AlC, Ti_3AlC_2 and Al_2O_3

were detected. Rietveld analysis of another sample, heated twice to 1550 °C in the DSC, yielded very similar results (Table 4).

A polished and etched OM micrograph of sample 3-9-HIP-1500 is shown in Fig. 12a. Comparing this figure with its XRD spectrum (Fig. 10c), three distinct phases can be identified. The white phase is TiC_x, the colored phase is Ti_3AlC_2 and the black phase, which is a minority phase, and barely registers in the XRD pattern, is the Al_2O_3 fibers. In previous work, we have shown that only when the Ti:A ratio is 3:1 does the etching result in vivid, multicolored grains.[78] We have also repeatedly shown that the easiest method to differentiate between the Ti containing MAX phases and TiC_y is to etch the samples: the latter shows up as a white, or bright phase.[79-80]. The polished and etched OM micrograph of sample 10-17-HIP-1300 (Fig. 12b) is also consistent with this notion. According to its XRD spectrum (Fig. 10a) the majority phase is Ti_2AlC, which turns brown upon etching. The colored phase is Ti_3AlC_2, and the dark, or black, areas are alumina. Note that the top and bottom areas in Fig. 12b are not etched.

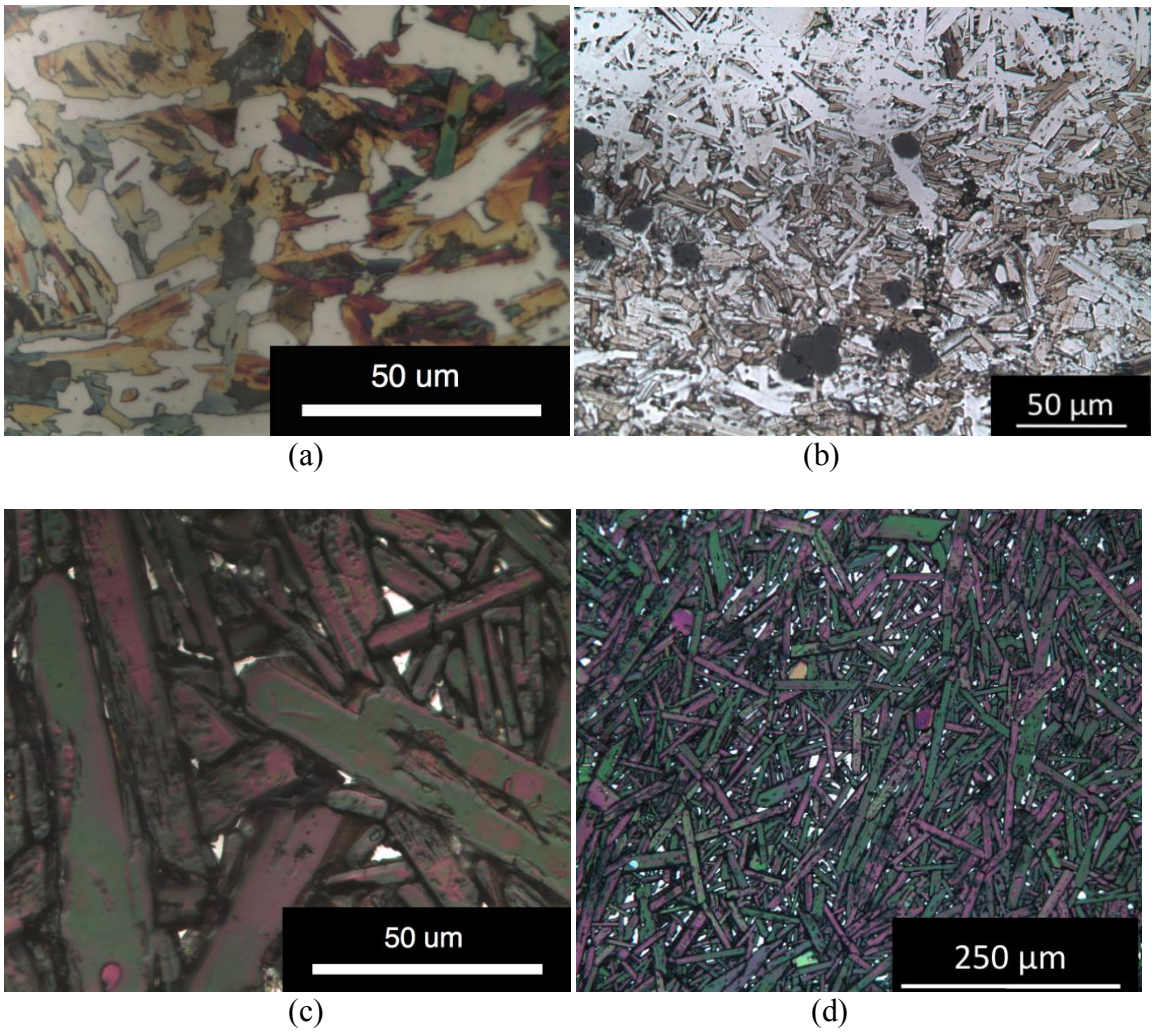

Figure 12: Polished and etched OM micrographs of sample; a) 3-9-HIP-1500. The multicolored phase is Ti_3AlC_2; the white phase is TiC_x; the dark regions are either porosity or Al_2O_3 fibers; b) 10-17-HIP-1300. The majority, brown phase, is Ti_2AlC and the colored phase is Ti_3AlC2. The 3 µm diameter Al_2O_3 fibers appear black. c) and, d) 10-9-HIP-1500. The majority colored phase is Ti_3AlC_2; the minority white phase, TiC_x.

The polished and etched OM micrographs (Figs. 12c and 12d) of sample 10-9-HIP-1500 also confirm the aforementioned conclusions. Consistent with its XRD pattern (Fig. 10b), the colored phase must be Ti_3AlC_2 and the white phase, TiC_x. Note that etching dissolves the Ti-aluminide phases, if present.

Based on backscattered electron, SEM images of sample 3-9-HIP-1500 (Fig. 13a), also shown in Fig. 12a, and the EDS results listed in the Fig. 13b, for the various locations labeled in a, four phases are identified; Ti_3AlC_2 (pts. 3, 9 and 11), Ti_3C_2 (pts. 7, 8 and 10) Al_2O_3 (pts. 1, 2 and 5) and a Ti-Si phase (pts. 4 and 6). As noted above, the contrast between TiC_x and Ti_3AlC_2 or Ti_3SiC_2 is weak in backscattered mode, which is why it is imperative to combine etched OM micrographs with the latter.

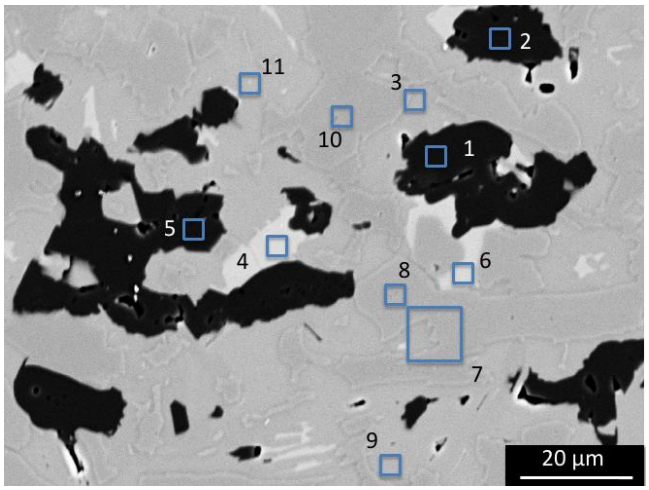

(a)

Atomic %

Point	Al K	O K	C K	Si K	Ti K	Phase
1	37.06	62.94	--	--	--	Al_2O_3
2	37.16	62.84	--	--	--	Al_2O_3
3	9.87	--	34.41	0.59	55.13	Ti_3AlC_2
4	2.86	--	8.11	32.28	56.76	$Ti_2Si(C,Al)$
5	34.29	61.15	2.15	1.15	1.26	Al_2O_3
6	2.5	--	9.46	32.88	55.17	$Ti_2Si(C,Al)$
7	3.99	--	38.22	--	57.59	Ti_3C_2
8	--	--	39.69	--	60.31	Ti_3C_2
9	16.08	--	30.76	0.74	52.42	Ti_3AlC_2
10	--	--	38.47	--	61.53	Ti_3C_2
11	16.06	--	28.43	0.86	54.66	Ti_3AlC_2

(b)

Figure 13: a) Backscattered electron, SEM image of sample 3-9-HIP-1500. b) Summary of EDS results for various locations labeled in a. Based on EDS results four phases are identified; Ti_3AlC_2 (pts. 3, 9 and 11), Ti_3C_2 (pts. 7, 8 and 10), Al_2O_3 (pts. 1, 2 and 5) and a Ti-Si phase (pts. 4 and 6). The Si comes from the borosilicate glass used to encapsulate the samples during HIPing (see below).

Figure 14a shows a low magnification backscattered SEM micrograph of the interface between sample 3-9-HIP-1500 (on right) and borosilicate glass (left). A higher magnification micrograph is shown in Fig. 14b. EDS results of the various numbered regions shown in Fig. 14b, are listed Fig. 14c. Based on these results the following phases/regions are identified: an Al_2O_3 layer, a boron-rich minority phase and borosilicate glass. (The boron and carbon concentrations should not be taken at face value, but are included for the sake of completion). Additionally a bright Ti-Si rich region, similar in composition to the bright areas found in Fig. 13 (e.g. pts. 4 and 6), is present.

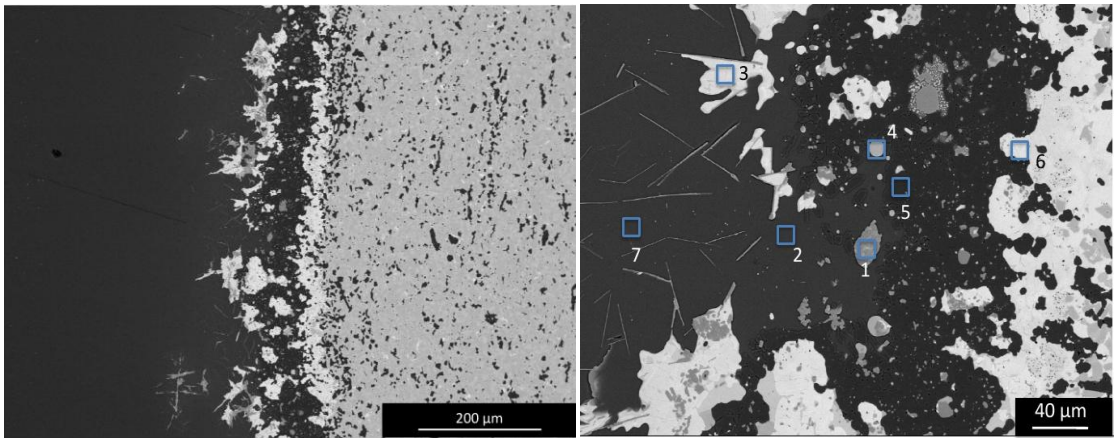

(a) (b)

Atomic %

Point	B K	C K	O K	Na K	Al K	Si K	K K	Ti K	Phase
1	58.61	4.64	--	--	--	13.3	--	23.46	B Rich
2	--	4.85	58.1	6.3	11.17	18.48	1.09	--	O Rich
3	--	8.66	--	--	--	36.17	--	55.18	Ti-Si
4	--	8.6	--	--	--	58.73	--	32.68	Ti-Si
5	--	--	60.51	--	39.49	--	--	--	Al_2O_3
6	--	12.73	--	--	1.31	33.9	--	52.05	Ti-Si
7	--	2.49	60.66	4.74	9.29	21.52	1.29	--	silicate glass

(c)

Figure 14: Backscattered electron SEM micrographs of sample 3-9-HIP-1500 near the borosilicate glass interface at, (a) low magnification and, (b) higher magnification. EDS results of the various numbered locations in the SEM micrograph are listed in table shown below the micrograph.

Figures 15a and 15b show how the fibers' microstructure changes between processing at 1300°C and 1500°C. When processed at 1300°C (Fig. 15a), the 10 μm Al_2O_3 fibers neither sinter together, nor appear to have reacted with the matrix, as greatly as they do at 1500°C (Fig. 15b).

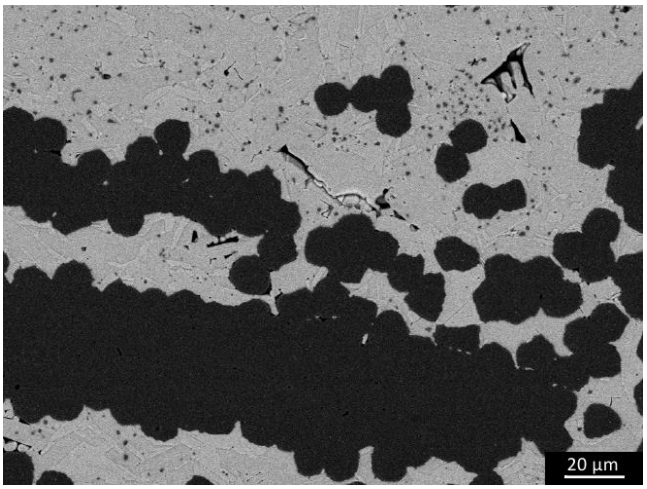

(a)

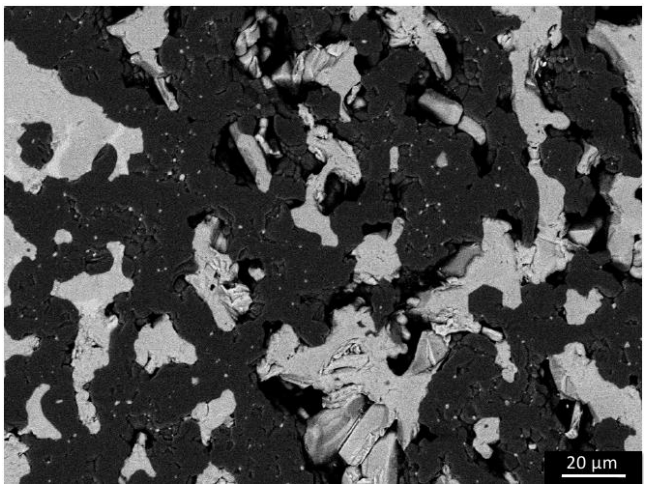

(b)

Figure 15: Backscattered electron SEM images showing effect of temperature on Al_2O_3 fiber morphology, for sample, a) 10-17-HIP-1300 and, b) 10-46-HIP-1500. The fibers in a appear to have retained their shape; those in b appear to have agglomerated and sintered together.

A typical TEM micrograph of a particle obtained from a sample of Ti_2AlC, without alumina, HPed at 1500 °C for 4 h is shown in Fig. 16a. The EDS confirming the presence of Ti, Al and C is shown in Fig. 16b. A selected area diffraction of the same particle (inset in Fig. 16) clearly shows the area imaged to be comprised of a large number of nano-grains or domains.

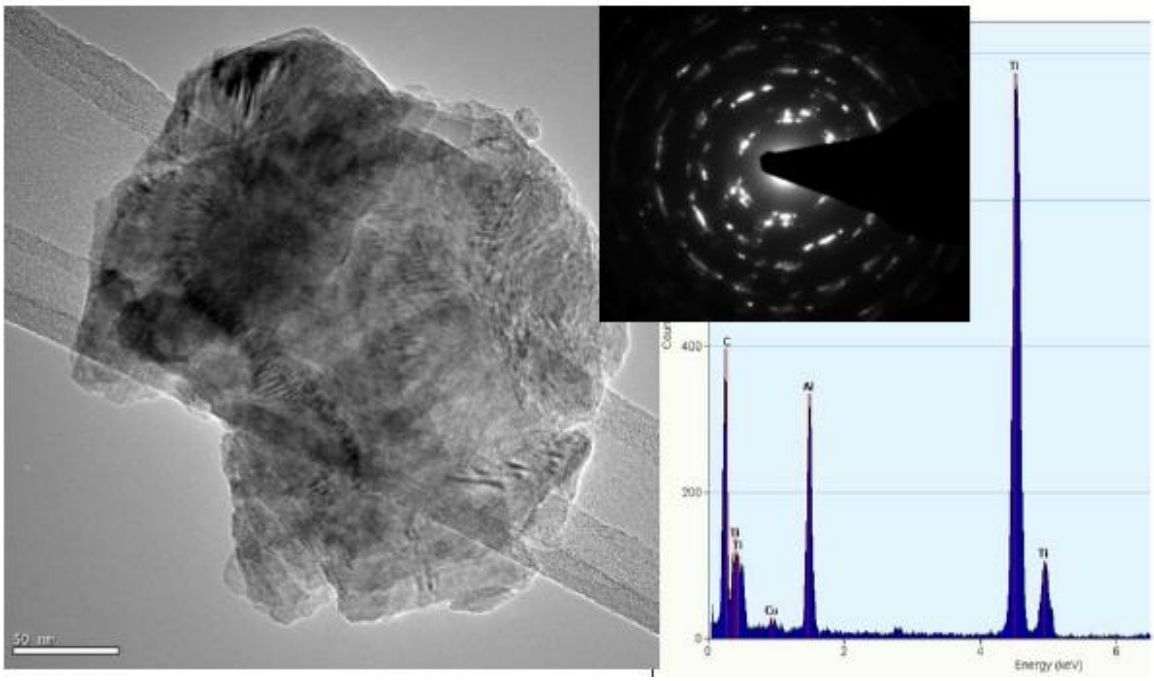

(a) (b)

Figure 16: a) TEM image of a typical Ti2AlC particle after heat treatment, showing multiple nanograins. b) EDS of particle shown in a indicating presence of Ti, Al and C. Top inset is selected area diffraction of same particle showing multiplicity of grains.

The DSC results of the 3:1 molar ratio Ti_2AlC:Al_2O_3 powder mixture, heated to 1410 °C, (Fig. 17a) are for the most part featureless. A small, but observable endothermic event at 1350°C during heating, which is also mirrored upon cooling, can be discerned. The TGA results of the sample heated to 1550 °C (Fig. 17b) show four regions of mass change: i) a

weight loss during the initial temperature increase, ii) a gradual mass gain until ≈ 1475°C, at which temperature mass is lost, iii) mass loss continues upon cooling reaching a minimum also ≈ 1475 °C, after which the sample gains weight down to ≈ 800 °C, after which it levels off. The concomitant mass spectroscopy results, also shown Fig. 17b, indicate the emission of several gaseous products such as CH_4, CO_2 and CO.

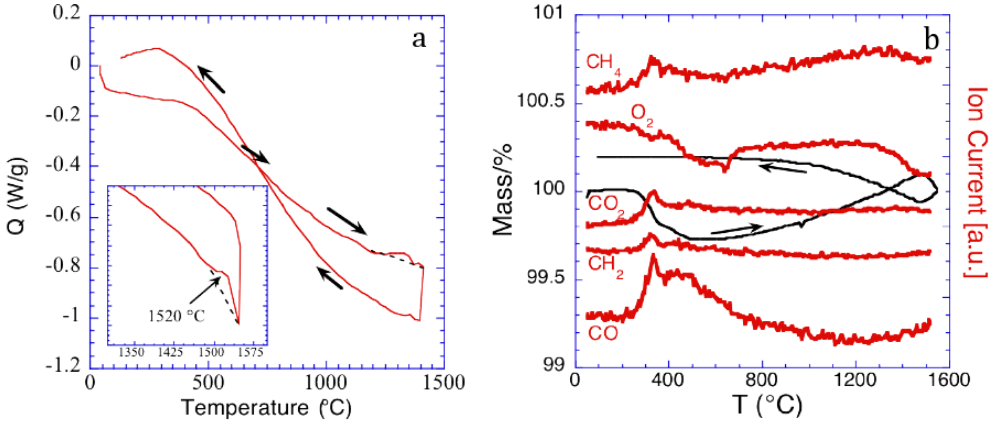

Figure 17: a) DSC of $3Ti_2AlC:Al_2O_3$ powder mixture heated to 1410 °C. A small endothermic peak registers at ~1350°C; on cooling a small exothermic peak is seen at around the same temperature. Inset shows DTA results of same composition heated to 1550 °C. A broad exothermic peak centered around 1520 °C is observed on cooling; b) TGA of sample heated to 1550 °C. Early mass loss is followed by mass gain and ultimately mass loss at T > 1450 °C. The gases evolved during heating are indicated on the figure.

2.1.4 Discussion

Based on the results presented above there is little doubt that at 1300 °C the Ti_2AlC structure is maintained (solid diamonds in Fig. 11) and that no reaction occurs between the fiber and matrix (Fig. 15a). Upon heating to 1500 °C, however, Ti_2AlC converts to Ti_3AlC_2 (Figs. 10 and 11) in a transformation that depends on temperature, time and "access" of Al to surroundings (see below). The question remaining is what are the operative reactions. One possibility is for Ti_2AlC to react with TiC and form Ti_3AlC_2.[81]

It is this reaction that most probably consumes the TiC present in the initial powder and thus explains why neither the samples HIPed at 1300 °C (Fig. 11) nor those heated in the DSC (Table 4) contained TiC. Note that after heating in the DSC the 211/312 ratio decreases from ≈ 5 to 3 (Table 4).

The amount of TiC in the initial powder, however, is insufficient to convert all the 211 to 312. At higher temperatures Ti_2AlC transform to Ti_3AlC_2 most probably according to the following simplified reaction:

$$2\ Ti_2AlC = Ti_3AlC_2 + TiAl_{1-x} + x\ Al\ (vap.) \qquad (2.1)$$

where $x < 1$. Note that the composition of the intermetallic formed depends on the amount of Al lost to the surroundings. If one mole of Al were lost, pure Ti would remain. However, before this can occur, the continued loss of Al should lead to the formation of TiC_x according to following simplified reaction:

$$Ti_3AlC_2 = Ti_3C_2 + Al\ (vap.) \qquad (2.2)$$

So the presence of TiC_y in the final composite (Figs. 10c and d) is not too surprising.

Reaction 2.1 is simplified in the sense that we are not allowing any non-stoichiometry in the Ti_3AlC_2 phase. Based on the various micrographs of the various samples (e.g. Fig. 9) it is clear that the volume fraction of the $TiAl_x$ phase is significantly less than it should be based on reaction 2.1. And while the exact reason for this state of affairs is not fully understood, one, or more, of the following two arguments can be invoked. First, the $TiAl_x$ – which is presumably a liquid at 1500 °C - is squeezed to the surface of the samples,

where it reacts with the surrounding glass in the HIP (see below) or the graphite foil surrounding the samples in the HP. The evaporation of Ti cannot be ruled out at this time.

Second, the Ti_3AlC_2 phase contains excess Ti and possibly C. This conjecture is consistent with the fact that the Ti/Al ratio of the Ti_3AlC_2 phase in Figs. 9 and 13 is closer to 3.3, than it is to 3. Given the difficulty of accurately quantifying the C-content in the EDS, more careful work is needed to explore whether the C/Al ratio also increases. The apparent Ti and C excesses can be explained by an Al deficiency in the A-layers as well as thickening of any TiC_y layers sandwiched between the Ti_3AlC_2 planes. A similar decomposition mechanism was reported for Ti_3SiC_2 (0001) thin films.[82]

The latter conclusion is also in tune with our understanding of how the MAX phases react. Given the chemical stability of the $M_{n+1}X_n$ blocks, and the fact that the A-layers are relatively loosely held, by now it is fairly well established that the most common reaction of the MAX phases is the selective loss/reaction of the A-group element. For example the MAX phases do not melt congruently, but decompose peritectically into $M_{n+1}X_n$ and the A-group element. The decomposition temperatures vary over a wide range; from ≈ 850 °C for Cr_2GaN [83] to above 2300 °C for Ti_3SiC_2.[84] The decomposition temperatures of the Sn-containing ternaries range from 1200 to 1400 °C.[85] Ti_3SiC_2 can be processed at 1600 °C in bulk form, but thin epitaxial films lose Si at temperatures as low as 1100 °C[82]. Heating Ti_3SiC_2 in a C-rich atmosphere results in the loss of Si and the formation of TiC_x.[86] When the same compound is placed in molted cryolite[78], or molten Al[87], essentially the same reaction occurs: Si escapes and TiC_y forms.

The effect of temperature on the transformation is best seen in Fig. 10; when the powder was HIPed to 1300 °C, there was little change compared to the initial powder (compare Figs. 8b and 10a). When the same powder was HIPed or HPed at 1500 °C for 4 h, it disassociated to Ti_3AlC_2 (Fig. 8a and Figs. 10b-d). After the two rapid consecutive DSC runs to 1410 °C and 1550 °C only a small fraction of the initial Ti_2AlC dissociated.

The evidence for the presence of an amorphous Ti-aluminide phase is multifold. It is clearly seen at the boundaries between the Ti_3AlC_2 grains (Fig. 9). A broad exothermic peak, centered around 1520 °C, is observed just upon cooling in the DTA (inset in Fig. 17a). Since no peaks belonging to any Ti-aluminide phases were observed in any of the XRD spectra they must be amorphous or nano-crystalline. Finally, a few Ti-rich nano particles, that SAD showed to be amorphous (not shown), were imaged in the TEM. In another region, an Al-rich, Ti-aluminide particle was found that was not amorphous. SAD showed it be the tetragonal intermetallic $Al_{0.64}Ti_{0.36}$ (ICSD-file 50-0726) with lattice parameter, a = b = 4.0296 Å; the c lattice parameter was 2.9561 Å.

Using the Scherer formula the average particle size of the Ti_3AlC_2 phase formed during the DSC run is estimated to be ≈ 12 ± 3 nm, a conclusion confirmed by TEM (Fig. 16 and its inset). This is an important result since it can explain both the general diminution of the MAX phase peaks upon heating, as well as suggesting a relatively easy method to produce nano-grains of the MAX phases. The very fine nature of the grains that form suggest that they formed by a nucleation and growth process. Had the 211 to 312 transformation occurred by a rearrangement of the number of TiC_x layers in between the

Al planes – i.e. by a topotaxial or intergrowth process - larger grains would most probably have formed.

The evidence for the loss of Al from the system is also clear and multifold. Given its low melting point relative to Ti it is likely that the majority of the weight loss at T > 1475 °C is due to the loss of Al. The initial weight loss during heating in Fig. 17b is due to the loss of moisture and other adsorbed gases from the powder compact. It is presumably the reaction between moisture and C in the compact that produces CH_4, CH_2, CO and CO_2. The weight gain between ≈ 800 °C and 1475 °C is presumably due to oxidation. Why that increases the oxygen concentration (Fig. 17b) however, is unclear. The relatively sharp mass loss around 1475 °C that continues as the sample is cooled (Fig. 17b) is presumably due to the loss of Al from the system. The reason Al or AlO were not detected by the mass spectrometer (Fig. 17b) is most probably due to the condensation of these gases in the tubes connecting the reaction chamber to the mass spectrometer.

Figure 14 not only shows that the Al is highly mobile, but, as important, that it reacts with the surrounding glass. Since alumina is thermodynamically more stable than silica, then the most likely simplified reaction is:

$$\text{boro-silicate glass} + y\text{TiAl}_2 = y\text{Al}_2\text{O}_3 + \text{TiSi}_z \qquad (2.3)$$

In other words, the Al reduces the Si in the glass. This reaction explains the presence of an almost continuous layer of both Al_2O_3 and $TiSi_z$ near the glass/sample interface (Figs. 14a and b). It also explains the presence of $TiSi_z$ pockets deep within the sample (Figs.

13a and b). Note that the morphology of the $TiSi_z$ phase formed (Fig. 13a and Figs. 14a and b) strongly suggests that it was liquid when it formed.

The results presented herein do not necessarily imply that Ti_2AlC is unstable at temperatures > 1400 °C. After all the first successful bulk synthesis of this compound was carried out by HPing elemental powders for 4 h at 1600 °C.[37] The answer to this apparent paradox, for which there is some confusion in the literature, has to do with the free energy change, ΔG, of reaction 2.1 or one that transforms Ti_2AlC to TiC_x directly. In an open system, where the activity of Al in the surroundings is vanishingly small, ΔG will be negative at all temperatures. In other words, the MAX phases are only kinetically stable. This is seen here in that the DSC sample rapidly heated to, and cooled from, 1550°C only marginally transformed to Ti_3AlC_2, while the sample heated to 1500 °C for 4 h did.

This insight also explains why samples in which the volume fraction of fibers was high tended to dissociate more. Presumably the fibers delayed densification long enough to allow much of the Al and Ti to escape into the vacuum of the hot press or react with the encapsulating glass during HIPing. The main evidence for this conjecture can be seen in comparing the SEM micrographs of sample 211-HP-1500 (Fig. 9) and 3-9-HIP-1500 (Fig. 13). In the both cases, the major phase present is Ti_3AlC_2, however, with the incorporation of fiber in the latter, no Ti-Al was found within the bulk of the sample.

The results presented herein suggest that alumina fibers can be used to reinforce Ti_3AlC_2 and/or Ti_2AlC, if the latter does not decompose (Fig. 15a). However, based on this work, 1300 °C may be near the maximum processing temperature, not because the fibers react with the matrix – they do not - but because at 1500 °C they sinter together (Fig. 15b) and presumably lose their load bearing capabilities. If more stable Al_2O_3 fibers can be found, the results shown here suggest that they can be used to reinforce Ti_2AlC and/or Ti_3AlC_2.

2.1.5 Summary and Conclusions

Fully dense, alumina fiber-reinforced composites can be fabricated, at temperatures as low as 1300 °C, by HIPing or HPing commercially available Ti_2AlC powders with 3-10 μm alumina fibers for 4 h. At 1500 °C, the alumina fibers sinter together and as importantly, the loss of Al to the surrounding results in the dissociation of Ti_2AlC into Ti_3AlC_2 and $TiAl_x$. If the loss of Al is severe, the ultimate phase remaining would be TiC_y. The loss of Ti by evaporation/reaction at 1500 °C cannot be ruled out at this time.

Since the MAX phases can only be kinetically stable when heated in an environment in which the activity of the A-element is vanishingly small, it is not surprising that the aforementioned transformation reaction is time, temperature and densification rate dependent. Low temperature, short times and rapid densification decrease the propensity of dissociation at high temperatures.

2.2 Ti_2AlC:SiC

2.2.1 Synthesis

Ti_2AlC powder [- 325 mesh, 3one2, Voorhees, NJ] was combined with 140 μm diameter SiC fibers [Avco Specialty Materials, Lowell, MA] or 10 μm diameter SiC fibers [Nippon Carbon Co. Ltd., Tokyo, Japan]. Hot-pressig (HPing) or hot isostatic pressing (HIPing) was used to densify the samples.

Techniques for combining the powder and fibers was completed in one of two ways; i) in situ layering of powder layers, interspersed with layers of 140 μm diameter fibers and, ii) dry mixing powder and 10 μm fibers in a plastic bottle.

Table 5: Summary of runs made with Ti_2AlC matrix and SiC fibers. Column 1 lists the fiber diameter, 211; column 2 the matrix/fiber molar ratio. The key to the label listed in column 7 is: fiber vol. fraction or blank when no fiber was added, followed by 211 (for Ti_2AlC powder), followed by consolidation method or DSC and last the processing temperature. The processing time was 3 or 4 h.

Fiber Dia. (μm)	Molar Ratio	Vol. %	Proc. Meth.	T (°C)	Time (h)	Label
N/A	N/A	N/A	HP	1400	3	211-HP-1400
10	3:1	12	HP	1400	3	12-211-HP-1400
10	16.4:1	2	HP	1400	3	2-211-HP-1400
140	12.3:1	3	HIP	1300	4	3-211-HIP-1300
140	3:1	9	HIP	1500	4	9-211-HIP-1500
N/A	2:1	16	DSC	1550	N/A	211-DSC-1550
N/A	2:1	16	DSC	1410	N/A	211-DSC-1410

HIP = Hot Isostatic Press
HP = Hot Press
DSC = Differential Scanning Calirometry
^ = Powder [Superior Graphite, Chicago, IL]

HIPed samples were first pressed into green bodies utilizing steel dies, 12.5 x 70 mm^2 in size, loaded corresponding to a pressure of 57 MPa for 60 s. Polyvinyl alcohol was added

as binder on an as needed basis (≈ 5 ml per 15 grams of powder). The green bars were embedded in a borosilicate glass powder [Fisher Scientific, Pittsburgh, PA] and brought to temperatures ranging from 1300-1500 °C at a rate of 10 °C/min and held for 4 h. The Ar pressure at temperature was 110 MPa.

The HPed samples utilized a graphite-heated hot press [Series 3600, Centorr Vacuum Industries, Somerville, MA] under vacuum of 10^{-2} torr, which was ramped at 500 °C/h to 1400 °C and held for 3-4 h under a pressure of 10-20 MPa. Green bodies were prepared directly in the 38 mm graphite dies that were used during synthesis according to previously described methods above.

Differential thermal analysis, DTA, was carried out on a 2:1 molar ratio of Ti_2AlC to SiC powders [Superior Graphite, Chicago, IL], in a He atmosphere. The powders were ball milled for ≈ 12 h and compacted into green bodies with a small pellet press. The latter were then heated at 20 °C/min up to 1410 °C or 1550 °C in a combined differential scanning calorimetry/thermogravimetric unit [Netzsch-STA 449 C Jupiter®, Selb, Germany]. The unit was also equipped with a mass spectrometer [Netzsch-QMS 403 C Aëolos®, Selb, Germany]. Each sample was heated twice to the same maximum temperature.

2.2.2 Characterization

For post synthesis characterization, the HIPed and HPed samples were filed using a diamond coated needle file into powders for X-ray diffraction (XRD) on a diffractometer [Model D500, Siemens, Karlsruhe, Germany]. In most cases, pure silicon, Si, powder (~10 wt. %) was added as an internal standard. Scans were carried out with Cu K_α radiation (40 kV and 30 mA) at rates of 1.2 or 2.4 deg (2Θ)/min, using steps of 0.02 and 0.04 deg, respectively.

For microstructural analysis, samples were cut with a precision diamond saw [Struers Accutom-5, Westlake, OH], mounted and polished to a 1 μm diamond suspension. Microstructure and elemental analysis were carried in a SEM [Zeiss Supra 50VP, Thornwood, NY] equipped with an energy-dispersive spectroscope (EDS) [Oxford Inca X-Sight, Oxfordshire, UK].

Selected surfaces were then etched with a 1:1:1 ratio of water and concentrated HF and HNO_3 for 5 s and immediately rinsed with water. The fiber/matrix interface was observed with an OM, [Olympus PMG3, Center Valley, PA or Keyence, VHX 600, Woodcliff Lake, NJ].

A TEM [FEI Tecnai, G2 TF 20, Hillsboro, Oregon] was also used on particles from the 2:1 pellets heated in the DSC. The TEM sample was prepared by dispersing powders in ethanol and depositing the solution onto a holey carbon grid.

2.2.3 Results

XRD spectra of the as-received powders and a bulk Ti_2AlC sample HPed at 1400 °C (211-HP-1400) are shown in Figs. 18 a and b, respectively. In both cases, the majority phase is Ti_2AlC. Rietveld analysis of the as-received powders (Table 4), however, indicated that the starting Ti_2AlC powder contained ≈ 19 mol.% TiC and ≈ 14 mol.% Ti_3AlC_2. The former two phases tend to react together to produce Ti_3AlC_2 at temperatures as low as 1300 °C[2]. Said otherwise, the starting matrix contained ≈ 15 mol.% Ti_3AlC_2.

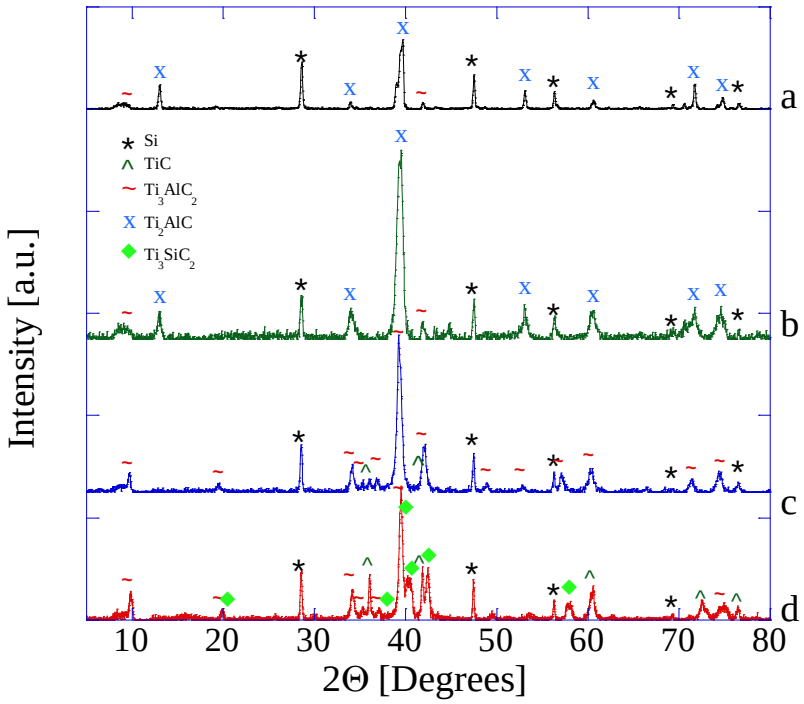

Figure 18: XRD spectra of (a) As received Ti_2AlC powder [3ONE2], (b) 211-HP-1400 (c) 2-211-HP-1400 and (d) 12-211-HP-1400. In all spectra ~ 10 wt. % pure Si powder was added for reference.

The XRD spectra of samples 2-211-HP-1400 and 12-211-HP-1400 are shown in Figs. 18c and 18d, respectively. Both samples were HPed at 1400 °C, but the latter had 6 times

more SiC than the former. In both cases, the major phase is Ti_3AlC_2. The sample with more SiC, however, not only contains more TiC_y, but the location of the most intense peak shifts towards Ti_3SiC_2. Both observations are more clearly seen when the foregoing spectra are superimposed on those of the powders ran through the DSC to 1550 °C (Fig. 19a). A perusal of these results establishes that: i) the DSC sample - a 2:1 molar mixture of Ti_2AlC and SiC powders - transformed to Ti_3SiC_2 and Al. This conclusion is confirmed and quantified in Table 6 (see below); ii) the sample containing 2 vol. % SiC, viz. 2-211-HP-1400, transformed mostly to Ti_3AlC_2; iii) sample containing 12 vol. % SiC, is in between the two.

Table 6: Summary of Rietveld analysis results of as-received $2Ti_2AlC$ + SiC powder mixture, and those of samples 211-DSC-1410 and 211-DSC-1550. The powder mixture was heated in the DSC at 20 °C/min to 1410 °C or 1550 °C and immediately cooled at same rate.

Phases	Molar Fraction	Lattice Parameters		Comments
		C (Å)	a = b (Å)	
2 Ti_2AlC + SiC as-received powder mixture				
Ti_2AlC	0.49	13.6946	3.0600	Goodness of fit; $\chi^2 = 5.82$
TiC_y	0.14	4.3093		
SiC	0.27	15.0750	3.0532	
Ti_3AlC_2	0.09	18.5400	3.0652	
2 Ti_2AlC + SiC powder mixture heated to 1410 °C				
Ti_3SiC_2	0.29	17.7022	3.0690	Goodness of fit; $\chi^2 = 3.82$
TiC_y	0.50	4.3310		
Al	0.17	4.0584		
Al_2O_3	0.03	12.9880	4.7787	
$Al_4O_{12}SiTi_2$	0.01	9.4460	3.8014	
2 Ti_2AlC + SiC powder mixture heated to 1550 °C				
Ti_3SiC_2	0.27	17.6877	3.0682	Goodness of fit; $\chi^2 = 4.23$
TiC_y	0.36	4.3257		
Al	0.30	4.0499		
Al_2O_3	0.06	12.8847	4.8091	
$Al_4O_{12}SiTi_2$	0.01	9.4745	3.7756	

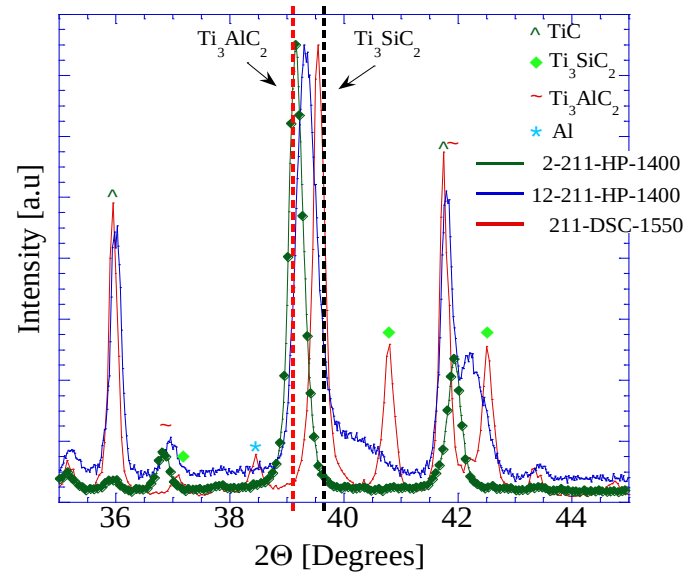

(a)

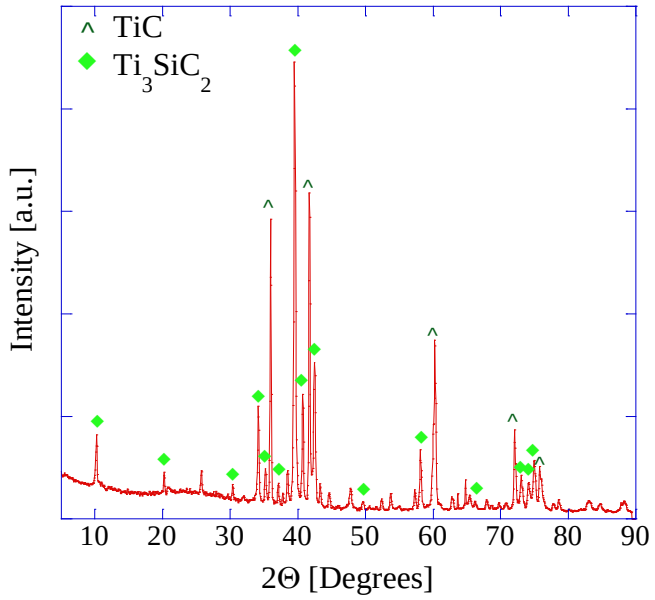

(b)

Figure 19: XRD pattern of, a) samples 2-211-HP-1400, 12-211-HP-1400 and the 2:1 molar ratio of Ti_2AlC and SiC powders used for thermal analysis. The red dotted line represents the 2Θ location of the most Ti_3AlC_2, intense peak; the black dotted line refers to the 2Θ location of the most intense Ti_3SiC_2 peak. One can observe that with an increase of SiC the strongest peak shifts from left (Ti_3AlC_2) to right (Ti_3SiC_2). (b) $2Ti_2AlC$:SiC powders heated to 1550°C in DSC.

The XRD diffraction spectrum of sample 211-DSC-1550 is shown in Fig. 19b. Summary of the Rietveld analysis - shown in Table 6 – confirm that the sample transformed to Ti_3SiC_2, TiC_y and Al. Traces of alumina and $Al_4SiTi_2O_{12}$ are also found.

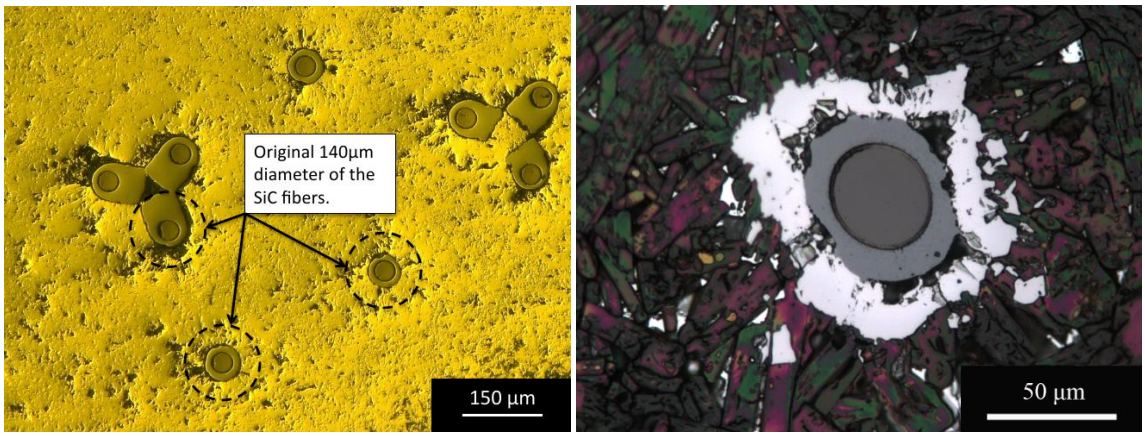

(a) (b)

Figure 20: OM micrograph of Ti_2AlC sample reinforced with 140 µm SiC. fiber; (a) 3-211-HIP-1300 in the as polished condition. (b) OM of 9-211-HIP-1500 etched with a 1:1:1 solution of water and concentrated HF and HNO_3 for 5 s. The white phase is TiC and the colored phase is $Ti_3(Si_{1-x},Al_x)C_2$.

A typical polished OM micrograph of sample 3-211-HIP-1300, reinforced with the 140 µm diameter SiC fibers, is shown in Fig. 20a; a polished and etched OM micrograph of sample 9-211-HIP-1500 is shown in Fig. 20b. Both micrographs clearly show that the 140 µm diameter of the SiC fibers was greatly diminished and resulted in the formation of a TiC layer – white phase in Fig. 20b – where the fiber used to be. Where the fibers clustered, (e.g. top left in Fig. 20a) the reaction is less severe and the initial fiber diameter is partially maintained.

A backscattered SEM micrograph of sample 9-211-HIP-1500 (Fig. 21a) shows the presence of 4 distinct regions that EDS (Fig. 21b) indicates are, from inside out: carbon,

SiC, TiC_x, with $x \approx 0.66$, and a $Ti_3(Al,Si)C_2$ solid solution. The EDS results are consistent with the fact that TiC_x etches white and the 312 phases color when etched[78-80] (Note that the Avco fibers are CVD fibers deposited on graphite cores). A fifth grey region (points 1 to 3) is an Al-rich layer containing Ti, with a Al:Ti ratio is ≈ 2.6.

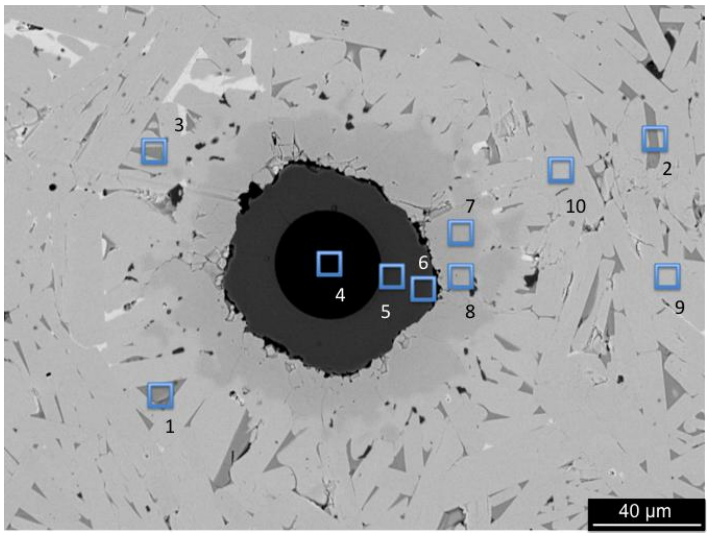

(a)

	Atomic %					
Point	C K	Al K	Si K	Ti K	O K	Phase
1	15.78	56.92	1.41	25.89	--	Al_2Ti, $Al_3Ti(C)$
1	9.95	64.43	1.47	24.15	--	$Al_3Ti(C)$
2	7.94	65.53	1.59	24.94	--	$Al_3Ti(C)$
3	9.46	64.7	1.12	24.71	--	$Al_3Ti(C)$
4	96.81	--	--	--	1.76	Carbon
5	51.5	--	48.5	--	--	SiC
6	51.53	--	48.47	--	--	SiC
7	40.57	--	--	59.43	--	Ti_3C_2
8	43.11	--	--	56.89	--	Ti_3C_2
9	30.69	14.23	2.48	52.6	--	$Ti_3(Al,Si)C_2$
10	31.23	13.84	2.78	52.15	--	$Ti_3(Al,Si)C_2$

(b)

Figure 21: a) Backscattered SEM image of sample 9-211-HIP-1500, b) EDS quantification of various regions marked in a.

EDS of a typical TEM micrograph of sample 211-DSC-1550 (Fig. 22) confirmed the solid solution nature of the $Ti_3(Al,Si)C_2$. Note that the Al/Si ratio is not uniform across the sample and that this particle is Si-rich as compared to those shown in Fig. 21.

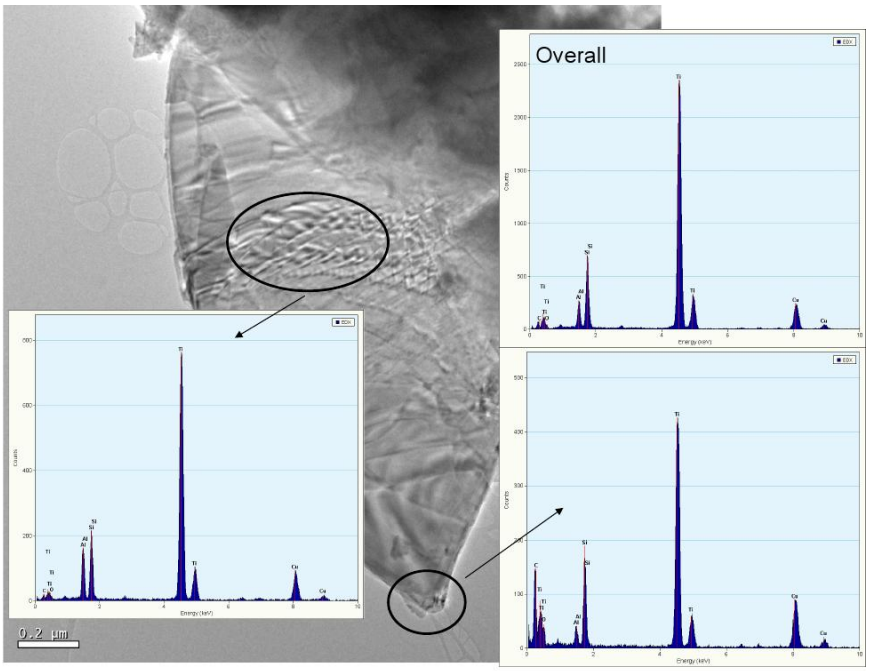

Figure 22: TEM micrograph of a single particle of 211-DSC-1550 sample heated to 1550°C. Inset shows the EDS spectra of the various regions marked.

The DSC results of the $2Ti_2AlC$:SiC mixture (211-DSC-1550) are shown in Fig. 23. The DSC run to 1410 °C (Fig. 23a), shows three specific events. Upon initial heating, there is an exothermic peak at ≈ 1160 °C, followed by an endothermic peak at ≈ 1230 °C. Upon cooling, a relatively small, exothermic peak is observed at ≈ 680 °C. In the sample heated to 1550 °C (not shown), the first two events are present, but with smaller intensities, and the event at 680 °C is absent.

The TGA data to 1550 °C (Fig. 23b) exhibits four regimes. An initial mass loss followed by an increase starting at a temperature of approximately 400 °C. This increase continues until 1450 °C, close to the maximum temperature of the experiment. At this point a mass loss begins and continues until the temperature reaches a maximum and then decreases again to 1450 °C. From 1450 °C to 950 °C mass is gained, after which no more weight changes are recorded.

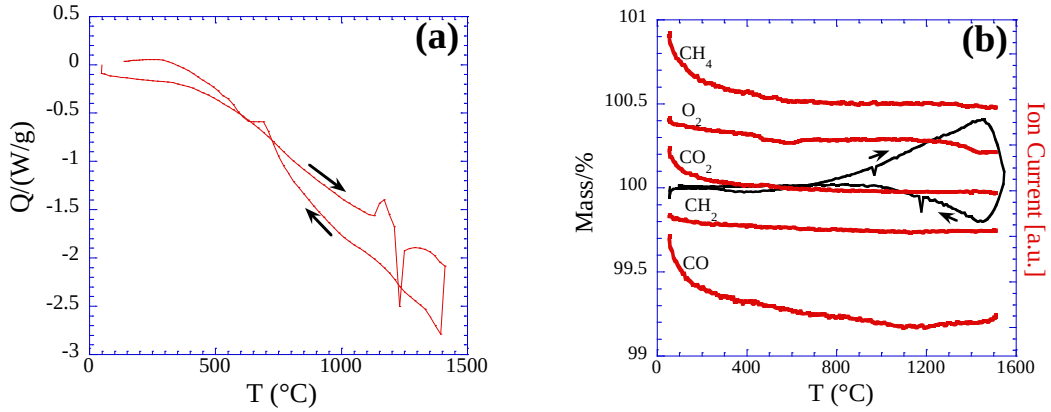

Figure 23: (a) The DSC data for $2Ti_2AlC$:SiC powders heated to a temperature of 1410°C and instantly cooled at the same heating rate, (b) shows the TGA data for the same compaction but to a max temperature of 1550°C with mass spectroscopy.

XRD of the powder (Fig. 19b), after the excursion to 1550 °C indicates the majority phases are Ti_3SiC_2 and TiC. The mass spectrometry data (Fig. 23b) indicate the existence of CH_4, O_2, CO_2, CH_2, and CO due a combination of air in the system and drying of the pellet.

2.2.4 Discussion

Based on the aforementioned results, it is reasonable to conclude that SiC reacts with Ti_2AlC according to the following, simplified reaction;

$$2\ Ti_2AlC + x\ SiC = Ti_3(Al_{1-x},Si_x)C_2 + Al_{1+x}Ti_{1-x} + x\ TiC \qquad (2.4)$$

where x ranges from 0 to 1. The reaction is simplified because it assumes the Ti to C ratio in TiC to be 1 and no loss of the Al to evaporation. Even in the absence of SiC, 211 still converts to 312, while rejecting a mole of Al and Ti atoms for every 2 moles of 211[2]. It is also important to note that the fraction of Si in the solid solution is a function of starting SiC content, i.e. x. At the x = 1 limit, pure Al is formed according to:

$$2\ Ti_2AlC + SiC = Ti_3SiC_2 + 2\ Al + TiC \qquad (2.5)$$

The presence of Al is clearly evidenced in the Rietveld analysis (Table 6) and the exothermic peak at 680 °C upon cooling from 1410 °C in the DSC (Fig. 23a).

The DSC results (Fig. 23a) suggest that reaction 2.4 is initially exothermic and starts ≈ 1170 °C. The endothermic peak observed at 1230 °C is presumably due to the melting of the Al when it comes out of the 312 lattice. To confirm this conjecture, the same sample was re-heated to 1410 °C a second time. The 1230°C endothermic peak was greatly diminished. Intriguingly, and for reasons that are unclear, a relatively large, double endothermic peak at ≈ 900 °C was observed upon re-heating. The origin of this peak, and why it does not occur at ≈ 680 °C, is unclear. Interestingly, upon cooling the second time, a clear peak at 680 °C is still clearly visible.

According to reaction 2.5, starting with a 2:1 Ti_2AlC:SiC molar ratio, should result in pure Al, Ti_3SiC_2 and TiC as observed (see Table 6). The a and c-lattice parameters of Ti_3SiC_2 are 3.0665 Å and 17.671 Å, respectively; the corresponding values for Ti_3AlC_2 are 3.075 Å and 18.578 Å. Based on the results listed in Table 6, it is obvious that the measured lattice parameters are closer to the former than the latter. The lattice parameters of TiC_y are a function of y. Based on the lattice parameter measured, viz. 4.089 Å (Table 6), and literature data[29] it is reasonable to assume y = 0.9.

For the other runs, x was < 1. In the latter situation a $Ti_3(Al_{1-x},Si_x)C_2$ solid solution, whose Si content scales with x is expected and observed. This is best seen in Fig. 19a, where the major 312 peak shifts from that near the location of the Ti_3AlC_2 peak to that of the Ti_3SiC_2 peak position with increasing x. In other words, the Si atoms prefer to be in the 312 structure than bonded to C in SiC.

The Ti-Al intermetallic phase appears at the grain boundaries (pts. 1-3 in Fig. 21). This phase, is similar in morphology and chemistry to that found when Ti_2AlC is heated to 1500 °C (Fig. 9) [2]. In other words, it is most likely a result of the dissociation of the Ti_2AlC, and not necessarily due to a reaction with SiC. Consistent with reaction 2.4, the intensities of the TiC_y peaks appear to increase with increasing SiC content (Fig. 19).

That a reaction occurs between the SiC fiber and Ti_2AlC to form TiC is clearly shown in Fig. 20. The original fiber diameter was 140 μm; after heating to a temperature as low as 1300 °C for 4 h, the fiber diameters were significantly reduced. Where the fibers bundle

together, they shielded each other from reaction and form 3-sided shapes as shown on the left in Fig. 20a. The etched OM micrograph, shown in Fig. 20b, further confirm the occurrence of a reaction. When etched, TiC_y is white, and the 312 MAX phases color[78-80]. The latter is confirmed because neither the 211 or 413 MAX chemistries color; only the 312's. The TEM/EDS micrographs, Fig. 22, of the DSC powders taken to 1550 °C confirm that a Si-rich solid solution forms. Interestingly upon cooling of the latter, no exothermic peak at 680 °C was observed. The most likely explanation is that at least a fraction of the Al evaporated as evidenced by the weight loss observed (Fig. 23b). Note that a weight loss is recorded in spite of the fact that the sample was oxidizing slowly – i.e. gaining weight - starting at about 800 °C.

2.2.5 Summary and Conclusions

HIPing or HPing, in the 1300-1500 °C temperature range, of Ti_2AlC powder with SiC fibers or powders resulted in fully dense composites. Based on the totality of our results we conclude that in the case of Ti_2AlC, the following reaction occurs:

$$2\ Ti_2AlC + x\ SiC = Ti_3(Al_{1-x},Si_x)C_2 + Al_{1+x}Ti_{1-x} + x\ TiC.$$

It thus follows that SiC fibers and/or powders cannot be used to reinforce commercially available Ti_2AlC powders.

2.3 Ti_3SiC_2:TiC:SiC

2.3.1 Synthesis

a. Bulk Ti_3SiC_2-TiC

Commercial Ti_3SiC_2 powder [-325 mesh, 3-ONE-2, Voorhees, NJ], which had approx. 16 vol.% TiC_x phase – calculated from post-synthesis image analysis – was HPed into a 63.5 mm diameter disc in order to establish a baseline. This fiber-free sample will henceforth, be labeled as 312-HP-1500. The raw powder was poured into a graphite foil lined graphite die and placed into the HP [Series 3600, Centorr Vacuum Industries, Somerville, MA]. The temperature in the HP was increased at a rate of 500 °C/h, to 1500 °C and held for 4 h in vacuum (10^{-2} torr). At temperature, a uniaxial pressure of 11.5 MPa was applied and held. After 4 h, the pressure was released and the sample was allowed to furnace cool.

b. Ti_3SiC_2:TiC:SiC Composites

The same Ti_3SiC_2 powder [-325 mesh, 3-ONE-2, Voorhees, NJ] was used to prepare two composite samples with the 140 μm diameter SiC fibers [Avco Specialty Materials, Lowell, MA]. Layers of fibers were produced by laying individual fibers in a mold. The mold was a slab of Al that had grooves spaced 200 μm apart. Fibers were then taped at the ends so a single layer, evenly spaced, could be incorporated into the powders. Each fiber plane, layer, was then interspersed with alternating layers of powder (see Fig. 25a).

Table 7: Summary of runs made with Ti_3SiC_2 matrix and SiC fibers. Column 1 lists the fiber diameter; column 2 the matrix/fiber molar ratio. The key to the label listed in column 7 is: fiber vol. fraction or blank when no fiber was added, followed by 312 (for Ti_3SiC_2 powder), followed by consolidation method, HP for hot pressing, and last the processing temperature. The processing time was 4 h.

Fiber Dia. (μm)	Molar Ratio	Vol. %	Proc. Meth.	T (°C)	Time (h)	Label
N/A	N/A	N/A	HP	1500	4	312-HP-1500
140	13.6:1	2	HP	1500	4	2-312-HP-1500
140	3:1	9	HP	1500	4	9-312-HP-1500

Samples were HPed in the same manner as the monolithic sample, in cylindrical graphite dies with diameters of 38 mm or 63.5 mm. Pressed to a uniaxial pressure of 11.5 MPa at a temperature of 1500 °C in a mechanical (10^{-2} torr) vacuum for 4 h.

2.3.2 Characterization

The microstructure of the Ti_3SiC_2:TiC, monolithic and the fiber/matrix interface of the Ti_3SiC_2:TiC:SiC, composite, samples were observed using an OM [Olympus PMG3, Center Valley, PA]. Samples were cut from the bulk with a precision diamond saw [Struers Accutom-5, Westlake, OH], mounted and polished to 1 μm diamond solution. In order to study the grain size, samples were then etched with a 1:1:1 combination of concentrated HNO_3:HF:H_2O and observed under an OM.

XRD was also completed to determine the phases present in the pre- and post-fabricated samples. The powders used for XRD were taken by filing with a diamond coated needle file. In most cases, 10 wt % pure silicon, Si, powder was used as an internal standard. Using an x-ray diffractometer [Model 500D, Siemens, Karlsruhe, Germany] scans were

made with Cu K_α radiation (40 kV and 30 mA) at rates of 1.2 or 2.4 deg (2Θ)/min, using steps of 0.02 and 0.04 deg, respectively

2.3.3 Results and Discussion

In contradistinction to Ti_2AlC discussed in section 2.2, the Ti_3SiC_2 powders do not react with SiC even at temperatures as high as 1500 °C. This is best seen when XRD spectra of the as-received powders and two samples (Fig. 24) – one with and the other without fibers - HPed to 1500 °C are compared. In addition to Ti_3SiC_2, the starting powder contained TiC_x. The resulting majority phases of both matrices of the monolithic Ti_3SiC_2 and fiber composite Ti_3SiC_2 samples are Ti_3SiC_2 and TiC_y.

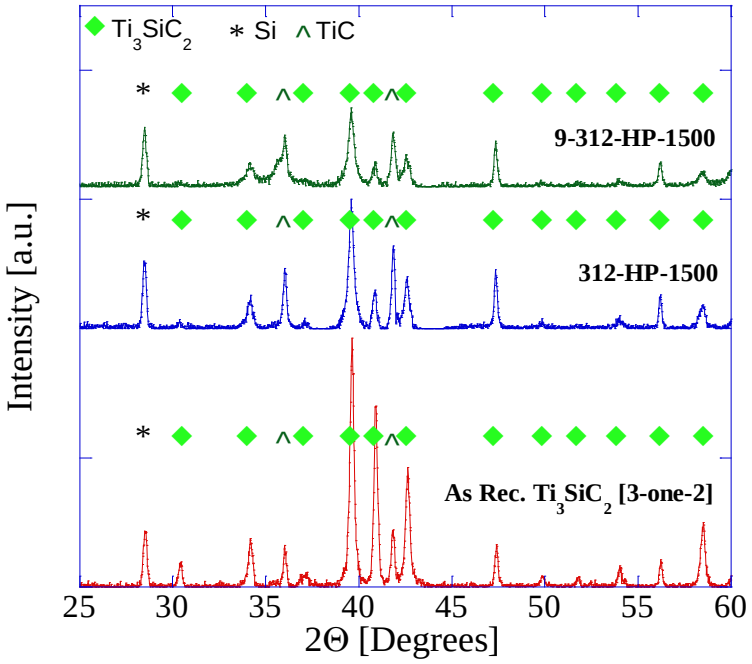

Figure 24: XRD of samples 9-312-HP-1500, 312-HP-1500 and Ti_3SiC_2 powder (as received from 3-one-2). Pure Si powder ~ 10 wt. %, was added as an internal reference.

The diffractogram (Fig. 24), shows a diminution in intensities of the Ti_3SiC_2 peaks similar to those in sections 2.1 and 2.2 (Figs. 10 and 18). The reason for this diminution in intensities is unknown at this time. The intensities of the TiC_y appear to stay relatively constant with respect to the added Si.

More direct evidence for the lack of a reaction is shown in OM micrograph (Fig. 25a and b) of sample 9-312-HP-1500. Unlike the fibers in the Ti_2AlC matrix (Fig. 20a and b), in this case there is clearly no reaction. The fiber/matrix interface is sharp and the fiber diameter is maintained at its original value of 140 μm. The Ti_3SiC_2 forms a dense matrix even in the case where the SiC fibers are only a few microns apart from one another, as can be seen in Fig. 25a.

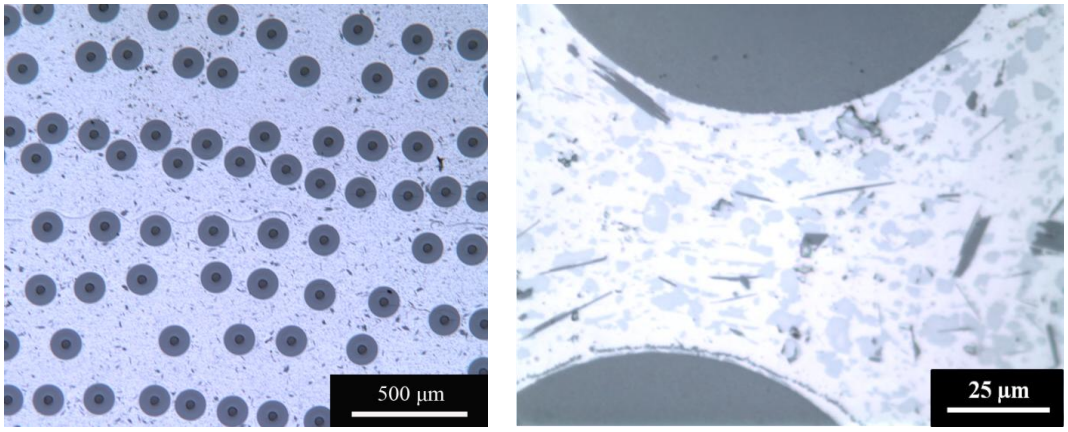

(a) (b)

Figure 25: OM of polished surface of sample 9-312-HP-1500. (a) at low magnification and, b) at higher magnification. Here the fiber and matrix do not interact and fibers/matrix interface is clean. Sample is dense and no porosity exists even when fibers are less than 100 μm apart.

In order to measure the grain size of the specimens, polished surfaces were etched with a 1:1:1 solution of H_2O and concentrated HF and HNO_3. A typical etched surface can be

found below (Fig. 26). Here again, the etched Ti_3SiC_2 grains color and the TiC_y grains etch white. This is consistent with the results found of the Ti_2AlC matrix samples, where the matrix transformed to Ti_3AlC_2 and TiC_y, (Fig. 12a). The average grain size was estimated to be 7±2 µm, with grains as large as 30 µm and as small as 2 µm. This structure falls in the fine-grained - FG or 3-5 µm - category, as defined by El-Raghy et al.[62]

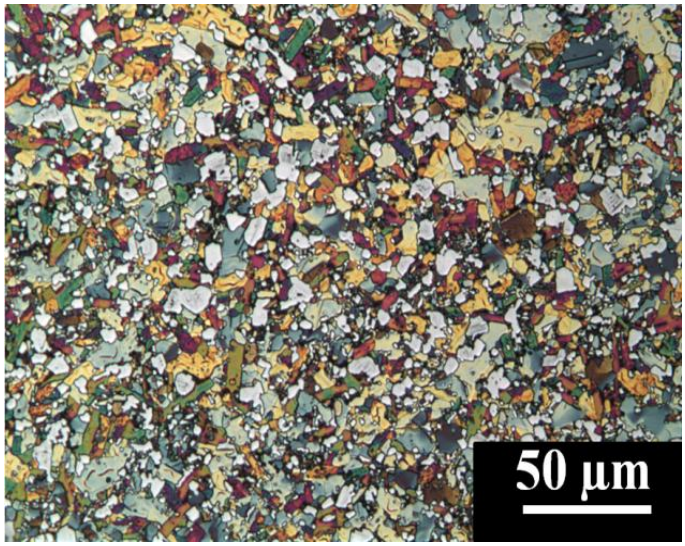

Figure 26: OM of sample 312-HP-1500, polished to 1 µm diamond solution and etched with a 1:1:1 solution of H_20:HF:HNO_3. Etching reveals the presence of both Ti_3SiC_2 and TiC grains, colored and white, respectively. OM imaging allowed for the grain measurement. Average Ti_3SC_2 grain size is 7±2 µm.

2.3.4 Summary and Conclusions

Fine grained, 7±2 µm, Ti_3SiC_2, with a secondary TiC_y phase, was HPed to full density, both as a monolithic bulk, and reinforced with 140 µm SiC fibers. In contrast to Ti_2AlC, no reaction is observed between Ti_3SiC_2 and SiC (see Figs. 20 to 25). This result in not too surprising since SiC is in equilibrium with Ti_3SiC_2[88]. This conclusion suggests that

SiC reinforced Ti_3SiC_2 matrix composites can be utilized as high temperature materials. The next stage in this research was to characterize the creep response of the composites and establish whether the addition of fibers enhances the creep properties.

CHAPTER 3. HIGH TEMPERATURE MECHANICAL RESPONSE RESULTS – CREEP

3.1 Set-Up and Parameters

The creep testing for this work was completed at Drexel University. The testing apparatus consisted of a furnace and a load cell that measured the applied force. A voltmeter and power-supply were used in union with the load cell in order to obtain accurate readings. The force in the system was applied by an air compressor and the strain was measured by a laser system made up of a laser transmitter and laser controller. A diagram of the set-up can be found below (Fig. 27). Samples were then affixed between the SiC rods by SiC pins that fit holes in the ends of dog-bone specimens (see below). This system is based on the one developed by Carroll and Wiederhorn for the high temperature testing of ceramics.[89]

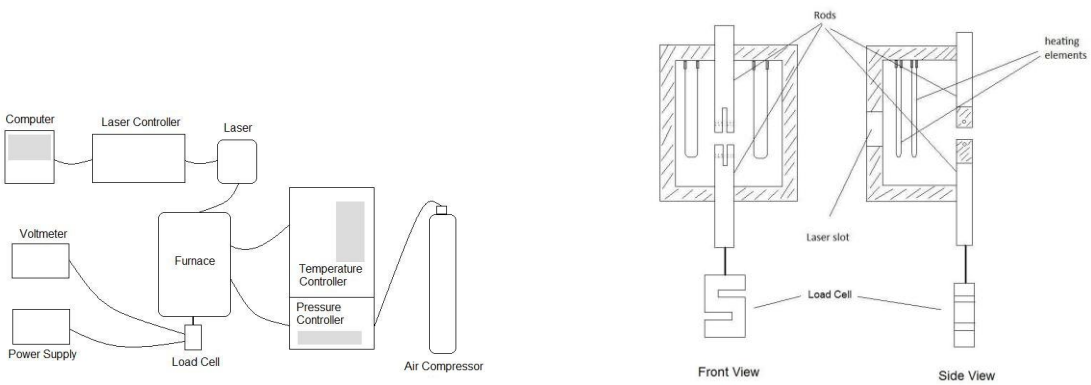

(a) (b)

Figure 27: Diagrams of creep testing equipment. (a) A general depiction of all points in the creep testing apparatus. (b) A more specific schematic of the inside of the furnace, showing the SiC rods in which the test specimen is placed.

Samples were prepared according to specifications set forth by the National Institute of Standards and Technology, NIST. In this work, we utilized SR30 and SR51 samples, whose dimensions are shown in Fig. 28a. Three specimens were successfully prepared at the Pennsylvania College of Technology [Williamsport, PA, USA] with wire electro-discharge machining, EDM, using regular carbide settings.

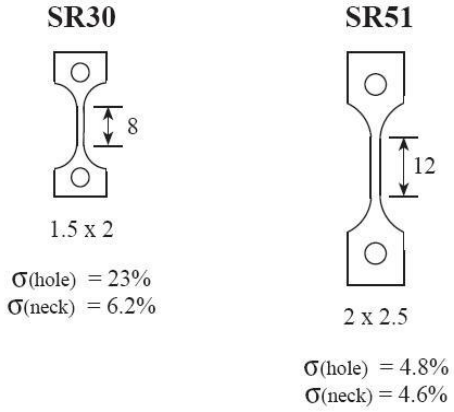

(a)

(b)

Figure 28: (a) Schematics of the dog-bone specimens used in this work. Dimensions are based on NIST standards for the high temperature, mechanical testing of ceramics. (b) Photograph of SR30 composite sample with champfered corners. Champfering was completed on SR30 samples in order to produce the maximum number of samples from bulk discs. Scale is in inches.

As stated above, strain was measured with the aid of a laser-system. SiC flags were attached to the gauge of the SR51 specimens, at a slight angle in order to lock them into position (Fig. 29a). During the experiments, the flags become permanently affixed to the sample due to the latter's oxidation. The SR30 specimens were too short to affix the flags since the SiC rods overlapped too far and the space available could not accommodate the SiC flags. In this case, the rods themselves were then used as markers, (Fig. 29b).

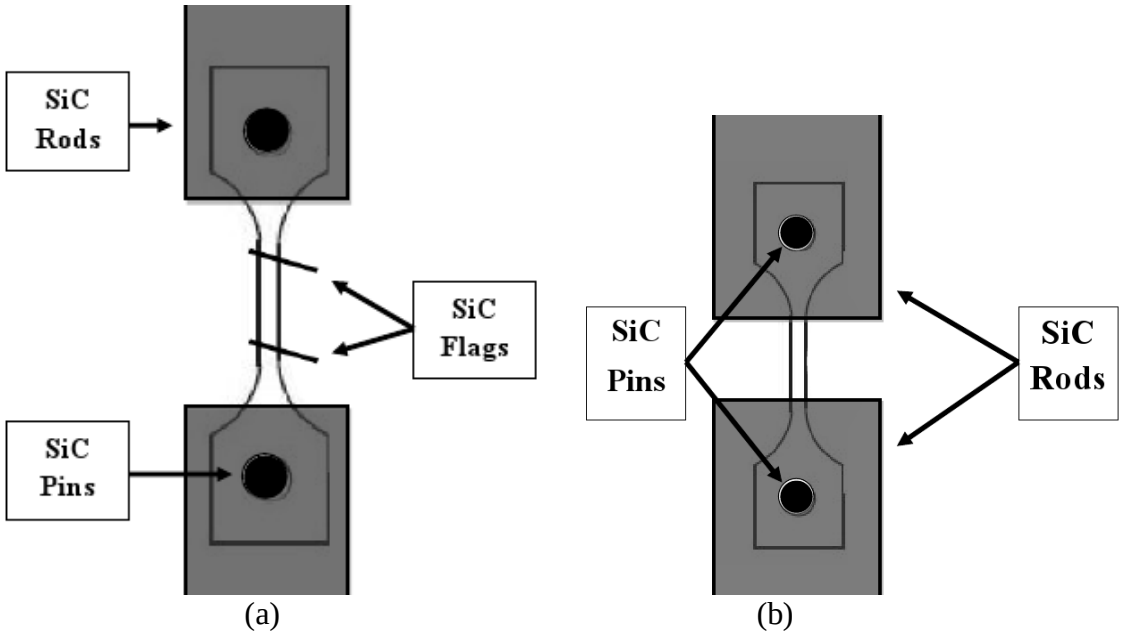

Figure 29: Schematic of test specimens seen in Fig. 28. (a) SR51 test specimen with attached SiC flags, used as guides for the laser extensometer to record the strain. (b) For the SR30 specimen, where the gauge length was too small to affix SiC flags, the SiC rods themselves were used instead as points of reference for the strain measurement.

The laser system measured the strain changes. In the case where SiC flags were used, SR51 specimens, the system would measure the difference in distance between the flags on the specimen. Where the SiC rods were used, SR30 specimens, the system would

measure the difference in distance between the rods. Then the laser system controller would calculate the strain change values by the data collected.

Before every experiment, the initial distance, L_o, between the SiC flags, or rods in the case of the SR30 specimens, was measured and programmed into the controller in order to zero out the calculation with the following equation:

$$\varepsilon = \frac{L - L_0}{L_0} \tag{3.1}$$

In Eq. (3.1), ε is strain, L is the distance change between flags, or rods, which is measured by the laser system every second.

3.2 Bulk Ti_3SiC_2:TiC Samples

Two tests were successfully completed on the Ti_3SiC_2:TiC sample, one SR30 and one SR51. Each test was completed using the same set-up. Once the specimen was placed in the apparatus, as discussed above, it was subjected to an initial load. The load, however, was nominal and only applied in order to maintain alignment of the specimen during set-up. The furnace chamber was then heated at a rate of 13.75 °C/min to a maximum temperature of 1100 °C. The specimen was then soaked at this maximum temperature for at least 75 min. After the soak, the pressure was increased from 20 MPa to 30 MPa to 40 MPa, taking approximately one minute to reach the chosen pressure.

The SR51 specimen was held at 40 MPa during the entire length of the test. The strain vs. time plot (Fig. 30) indicates that the specimen failed after 52.1 h at a strain rate of ≈ 8.1×10^{-9} s^{-1}. The strain rate was determined by sampling the data in the middle of the

strain vs. time curve, in order not to get the data mixed with the initial loading or the failing region of the plot.

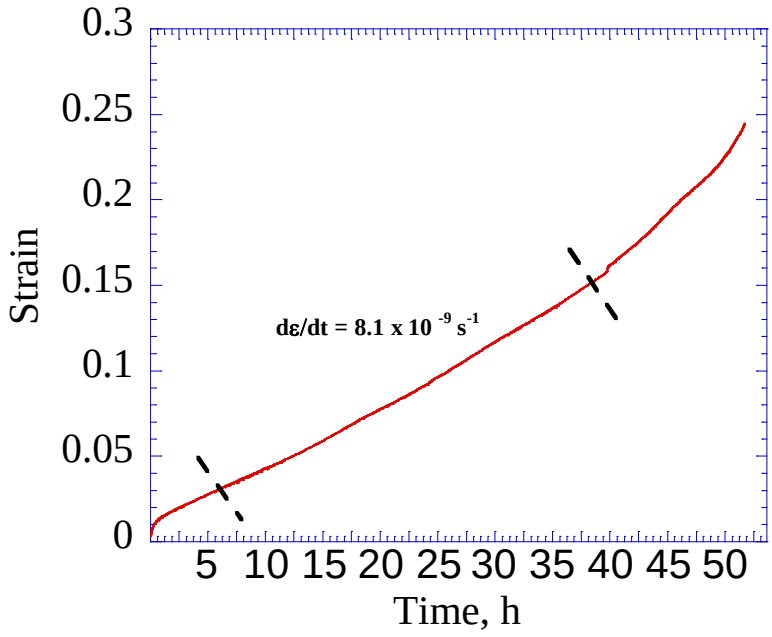

Figure 30: Tensile creep strain vs time of bulk Ti_3SiC_2:TiC test specimen SR51. Test was carried out at 1100 °C at a constant σ = 40 MPa. When secondary creep, region between the two angled dotted lines, is analyzed, the strain rate is found to be 8.1 x 10^{-9} s^{-1}.

A second test was run on a SR30 specimen. After a temperature of 1100 °C was reached, a load of 20 MPa was applied and held for 22 h after which it was increased to 30 MPa for 42 h and finally 40 MPa where it was held till failure, for a total of ≈ 93 h. Each load produced a different strain rate; 3.9x10^{-7}, 8.1x10^{-7} and 2.2x10^{-6} s^{-1} for the 20, 30 and 40 MPa loads, respectively.

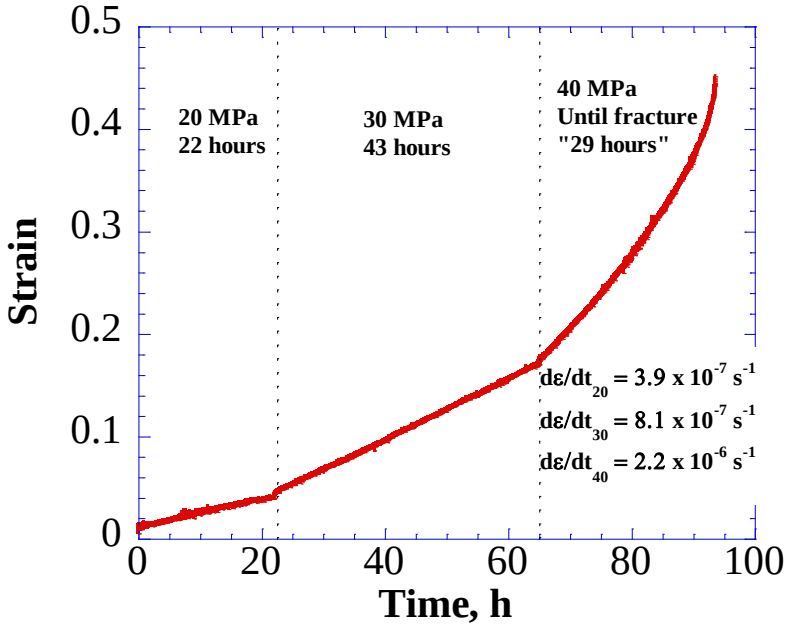

Figure 31: Tensile creep strain vs time for bulk Ti_3SiC_2:TiC SR30 specimen. Testing was carried out at 1100 °C, but at varying loads. For the initial 22 h, σ = 20 MPa, followed by an increase to σ = 30 MPa for 42 h and finally the load was taken to σ = 40 MPa till failure, totaling 93 h. Strain rates were measured for the 20, 30 and 40 MPa loads as 3.9 x 10^{-7}, 8.1 x 10^{-7} and 2.2 x 10^{-6} s^{-1}, respectively.

3.3 Ti_3SiC_2:TiC:SiC Composites

One test was successfully completed on a SR30 Ti_3SiC_2:TiC:SiC composite sample. Once the specimen was placed in the apparatus, as discussed above, it was subjected to an initial load. The load, however, was nominal and only applied in order to maintain alignment of the sample during set-up. The furnace chamber was then heated at a rate of 13.75 °C/min to a maximum temperature of 1100 °C. The specimen was then soaked at this maximum temperature for at least 75 min. After the soak, the pressure was applied to 20 MPa and then 40 MPa, taking approximately one minute to reach the chosen pressure.

When the applied load corresponded to 20 MPa – held for 118 h (Fig. 32) – the strain rate was 8.9 x 10^{-8} s^{-1}. At the end of this stage, the specimen had strained to about 4 percent. However, the specimen failed shortly after, approx. 14 h, at 40 MPa. A useful strain rate was not measured in this region because of the extensive strain and a weakened structure.

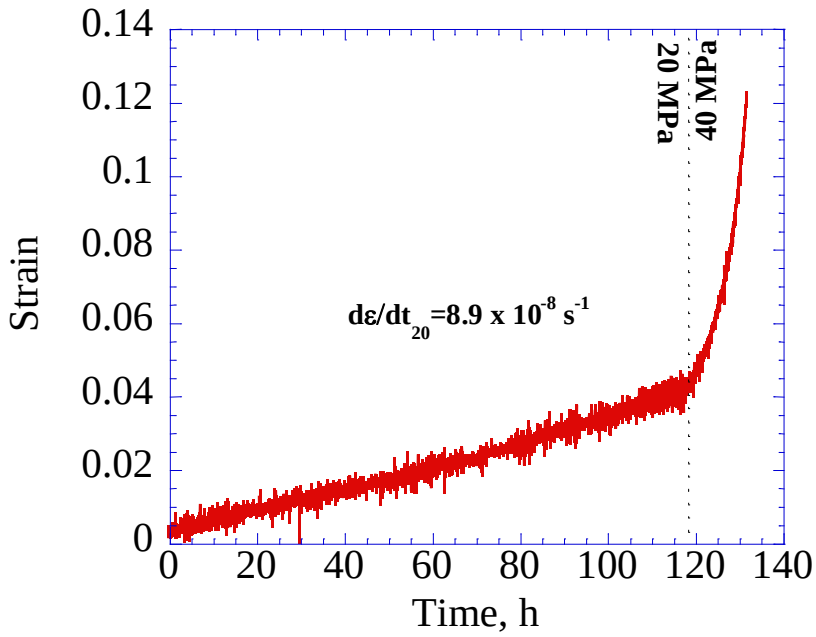

Figure 32: Creep strain vs time at different loads at 1100 °C for Ti_3SiC_2:TiC:SiC, composite, SR30 specimen. For the initial 118 h σ = 20 MPa, followed by an increase to σ = 40 MPa, till failure, ~ 14 h after load increase. Strain rate for the 20 MPa region was calculated to be 8.9 x 10^{-8} s^{-1}.

3.3.1 Microstructural Characterization of Fracture Surface

Below are secondary SEM images of both fractured surfaces.

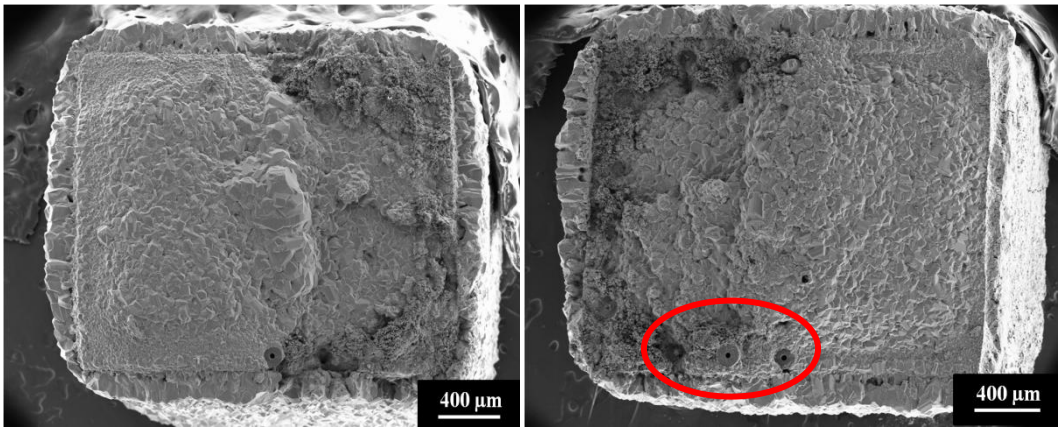

(a) (b)

Figure 33: (a) and (b) SEM, secondary electron, images of the SR30 composite specimen's fracture surfaces. Surface was extensively oxidized. Circled in the bottom left hand corner, in red, on b are three SiC fibers.

Figure 33 clearly shows extensive surface oxidation of the two halves. The oxidation covers most of the fiber surfaces and therefore it is difficult to analyze the failure mechanism. Fibers encompass only one half the cross-sectional surface, which can be observed clearly in Figs. 37a and 38a-b. This being the case, it is logical that half of the fractured surface, the half that was not reinforced – the left and right sections of Fig. 33a and b, respectively – failed before the reinforced area and thus was exposed to the environment longer and oxidized uniformly when compared to the right and left sections in Figs. 33a and b, respectively. Several fibers are apparent and can be seen, circled, in the bottom of Fig. 33b. Figure 34, below, further explores this area.

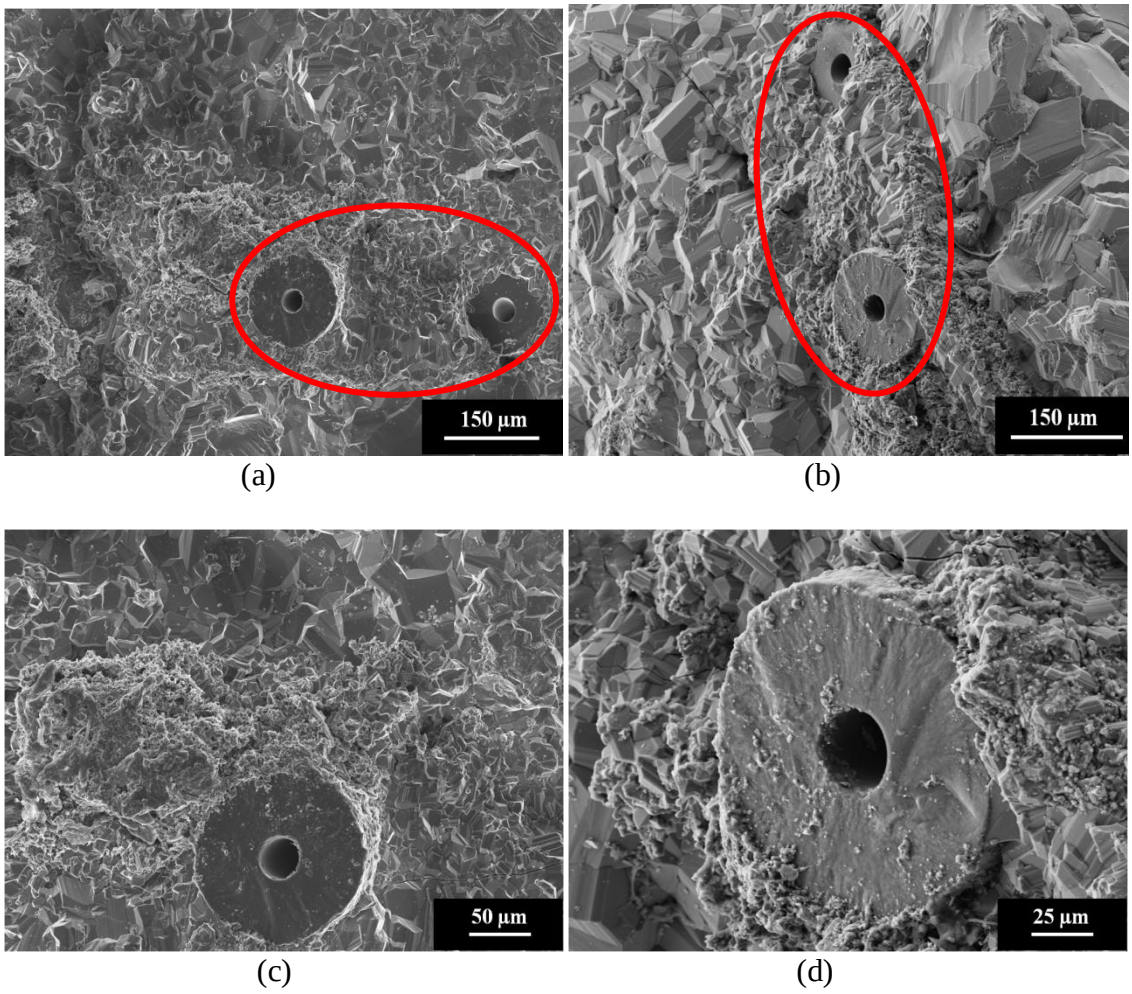

Figure 34: SEM secondary electron images of the fibers seen, circled in Fig. 33. (b) and (d) are tilted images of (a) and (c). The fibers in b are clearly at different levels. The fiber seen in b and d is the cleanest fiber found for analysis. The fiber can be clearly seen offset from the matrix surface. These two observations suggest at least some fiber pull-outs.

Fibers of interest in Figs. 34a and b are at different heights with respect to one another. Fig. 34d is a tilted secondary electron SEM image of the fiber seen in Fig. 34c. As can be seen, the fiber is offset from the matrix interface. It is clear that all fibers are not at the same depth in comparison to the matrix surface, which suggests at least some pullout. At this time, there is no conclusive evidence to state if pullouts were in effect, or if the fibers being outset from the matrix surface is due to the oxidation of the fracture surface after

failure. It is our contention that fiber pullout aided in the additional strengthening of the composite and thus increased the time to failure and decreased the strain rate of this specimen.

3.4 Discussion

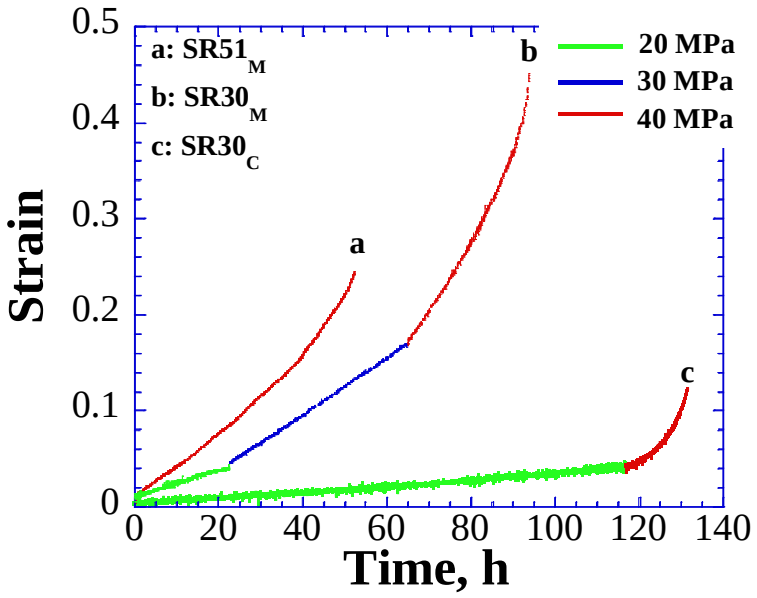

Figure 35: Tensile creep strain vs time for all three tests. This overlain plot easily shows the improvements the SiC fibers, line c, is for the Ti_3SiC_2:TiC matrix, lines a and b.

Figure 35 compares the three successful creep tests. This comparison makes it easy to see the improvements made to both the time to failure, t_f, and to the total strain to failure of the Ti_3SiC_2 matrix. The most important of these comparisons is the first segment of the 20 MPa portion of line b (monolithic), and the 20 MPa portion of line c (composite) – both in green – shows the extent of the improvement. While the monolithic sample

reached a strain of roughly 4 % in 22 h, the composite sample did not reach a strain of 4 % until after 118 h.

Further confirmation of the impact of the fibers can be obtained by comparing the results obtained herein to those of Radovic et al.[90] on FG Ti_3SiC_2. Radovic et al. tested Ti_3SiC_2 at varying temperatures, one of them being 1100 °C. When the data from the experiments of this work are overlain in Fig. 36 they fall within reason to the 1100 °C line. This plot compares the creep rate, s^{-1}, of varying test specimens with respect to testing temperature, °C, and applied stress, MPa. With increasing temperature and stress, the strain rates of the FG Ti_3SiC_2 samples will also increase. This is none too surprising.

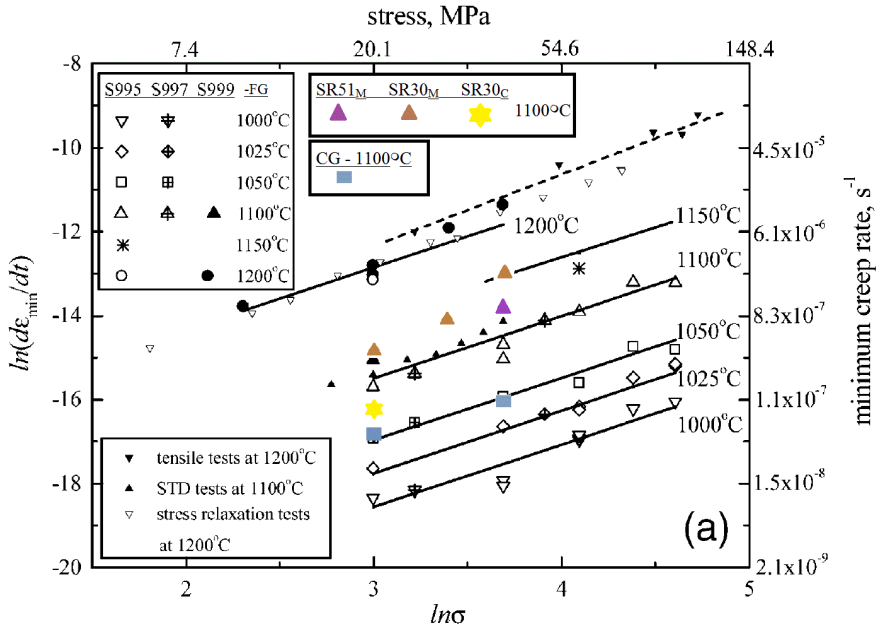

Figure 36: A log-log plot of creep strain rate vs stress. This original plot is taken from the work by Radovic et al.[90] on FG Ti_3SiC_2. The results from this work on both a monolithic matrix of Ti_3SiC_2:TiC and a composite of Ti_3SiC_2:Ti:SiC have been overlain. The brown triangles represent the monolithic SR30 specimen tested at T = 1100 °C and σ = 20 and 40 MPa. These fall very close to the data Radovic et al. published at this same T and σ. The yellow star, is the composite specimen tested at T = 1100 °C and σ = 20 MPa. This is still within reason of the Radovic et al. data, but shows a definite reduction in strain rate.

In addition to the fractured surface presented in Figs. 33 and 34, cross-sections were taken from the gauge of both the monolithic and composite specimens, right below the fracture surface. These specimens were mounted, polished and imaged with both OM and SEM with secondary and backscattered electrons.

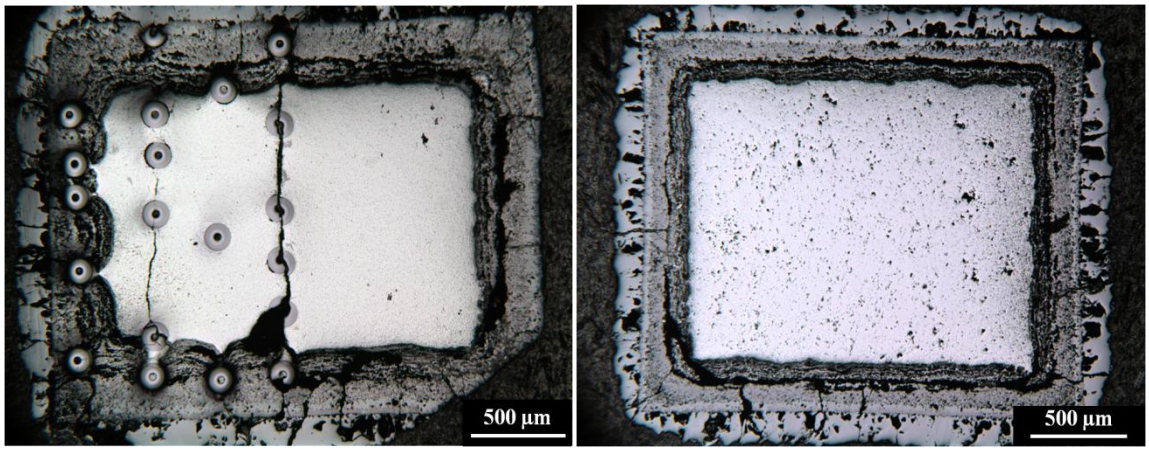

(a) (b)

Figure 37: OM imaging of the polished cross-section just below the fracture surface of, (a) composite SR30 specimen, at T = 1100 °C for ~132 h, and bulk SR30 specimen, at T = 1100 °C for ~93 h. Oxidation is clearly seen in both samples.

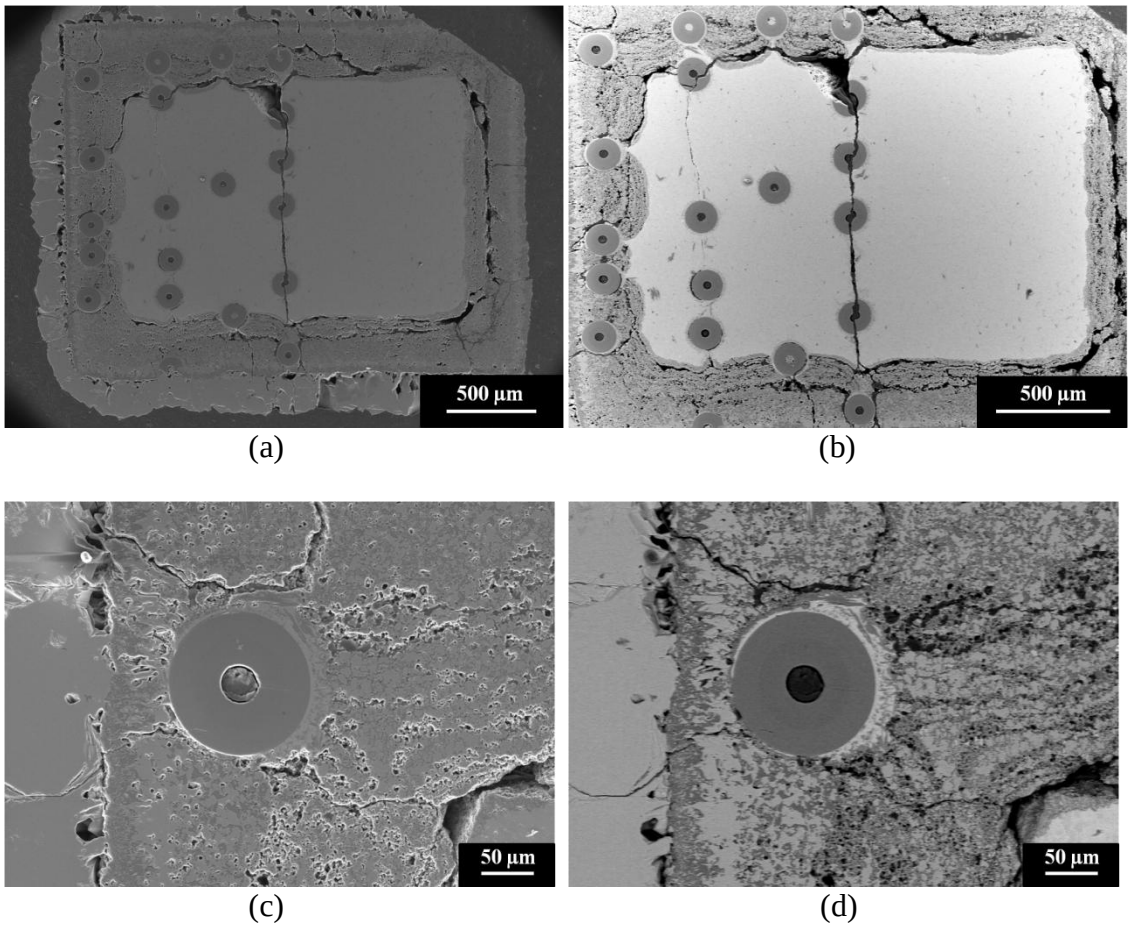

Figure 38: SEM of cross-section of SR30 composite specimen, (a) a secondary electron SEM image of the entire cross-section with the backscattered image shown in (b). (c) Secondary electron SEM image of just one fiber within the inner oxide layer, with a backscattered electron SEM image shown in (d).

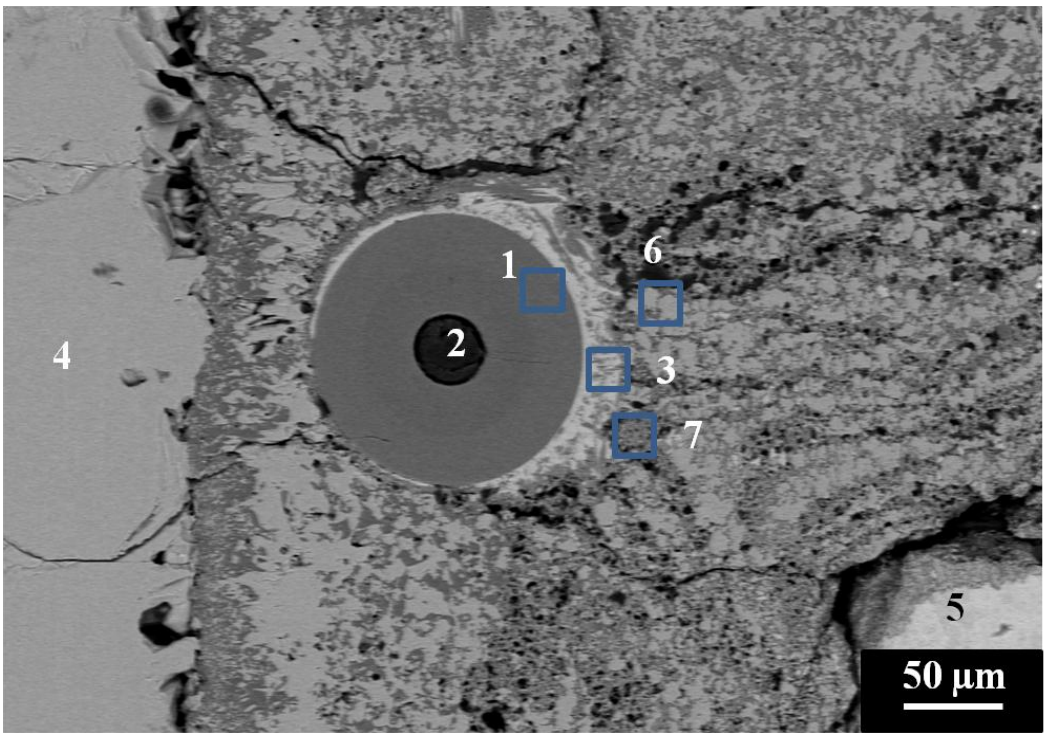

(a)

Spot	Atomic %			
	C K	O K	Si K	Ti K
1	29.07	--	70.93	--
2	82.61	17.39	--	--
3	3.83	--	53.41	42.76
4	--	45.09	--	54.91
5	15.17	--	13.64	71.19
6	--	39.97	--	60.03
7	--	--	91.67	8.33

(b)

Figure 39: (a) SEM, backscattered image of Figs. 38c-d. Several regions have been identified with the use of EDS; the results shown in (b). Although, EDS was not calibrated for accurate measuring, the data is shown for comparison. Three major regions are identified. The outermost region, spot 4, is made up of Ti and O. The middle layer, spots 6 and 7, is made of Ti, Si and O. And the inner layer, spot 5, is Ti, Si and C. These results agree with the literature that show that the oxidation of Ti_3SiC_2 occurs by the formation of an outer TiO_2 and an inner, or middle layer, of TiO_2 and SiO_2[63].

The above micrograph and table, (Fig. 39), show the results of energy dispersive spectroscopy, EDS, completed on the polished surface. These results agree with the literature that show that the oxidation of Ti_3SiC_2 occurs by the formation of an outer TiO_2

and an inner, or middle layer, of TiO_2 and SiO_2[63]. It is important to note that the EDS measurements were not calibrated when Fig. 39 was obtained. Therefore the measurements are slightly out of proportion. The purpose of this figure is only to show that, point 4, in the outer scale, does appear to be made up TiO_2 and that points 6 and 7 are comprised of Ti, Si and O.

3.5 Summary and Conclusions

Monolithic and composite samples were hot pressed to 1500 °C for 4 h with starting materials of: a) Ti_3SiC_2:TiC_x powder and, b) Ti_3SiC_2:TiC_x powder and 140 µm SiC fibers, respectively. Test specimens were machined, using EDM, into dog-bones to NIST standards, SR30 and SR51. Creep tests were completed at 1100 °C and stresses of 20, 30 and 40 MPa. Tests were run until failure, which was followed by post-creep microstructure analysis with the aid of OM and SEM, with EDS.

The creep results of the SiC fiber-reinforced composite showed a decrease in strain rate when compared to both the literature[90] and those carried out on monolithic samples made in this work. It is concluded that continuous, SiC fibers, 6.3 vol.%, increase the high temperature creep resistance of a Ti_3SiC_2:TiC matrix.

CHAPTER 4. SUMMARY AND CONCLUSIONS

4.1 Summary and Conclusions

The work presented above evaluated several possible MAX phase/ceramic fiber composites, namely: Ti_2AlC:Al_2O_3, Ti_2AlC:SiC and Ti_3SiC_2:TiC:SiC. Varying results were observed, some of which were initially surprising. The first reaction pair, Ti_2AlC:Al_2O_3, was processed by HIPing and HPing Ti_2AlC powders and 3-10 µm alumina fibers to temperatures of 1300-1500 °C for 4 h. At 1300 °C fully-dense, microstructurally sound composites were produced. However, at 1500 °C the alumina fibers agglomerate and, more importantly, Al was lost to the environment, converting the Ti_2AlC, to Ti_3AlC_2 and $TiAl_x$. Therefore this combination may produce a viable composite, but only at T < 1300 °C.

The second combination, Ti_2AlC:SiC, was produced by HIPing and HPing Ti_2AlC powder and 140 µm SiC to temperatures of 1300-1500 °C for 4 h. At the maximum temperature, 1500 °C, the matrix forms Ti_3AlC_2 and $TiAl_x$. However, in addition to this reaction, at both temperatures, 1300 and 1500 °C, the SiC fibers and matrix also reacted forming a solid solution according to the following equation:

$$2\ Ti_2AlC + x\ SiC = Ti_3(Al_{1-x},Si_x)C_2 + Al_{1+x}Ti_{1-x} + x\ TiC$$

Note that at x = 1, Ti_3SiC_2 and pure Al are formed. Therefore, this combination is not a suitable composite at temperatures high enough to produce fully dense matrices.

Finally, it was shown that the combination of Ti_3SiC_2:TiC:SiC produced a viable composite that was fully dense with a matrix/fiber interface that was clean and reaction

free. Dog-bone tensile samples, conforming to NIST standards for SR30 and SR51 specimens, were EDMed for both the monolithic, Ti_3SiC_2:TiC, and composite, Ti_3SiC_2:TiC:SiC samples. Even at ≈ 6 vol. %, the creep resistance at 1100 °C and 20 MPa for the composite was better than the monolithic specimens made with the same powders. Although the improvement of the high temperature mechanical properties of Ti_3SiC_2 shown is not groundbreaking, it is significant and convincing enough to instigate further research.

4.2 Future Work

This work opens the doors to the promising field of ceramic fiber-reinforced MAX phase composites, which had not been previously explored. Although this work is a good start, there is much to still be completed. It is the author's recommendation that more work is needed with respect to several topics:

- The reaction combination of Ti_3SiC_2:TiC:SiC showed an increase in time to failure with only 6.3 vol.% fiber located in only one half of the cross-section. Work is needed to produce samples with higher loadings of fibers, and a more effective method of dispersing these fibers in the matrix.
- A pure Ti_3SiC_2 matrix is recommended for further study. Although the Ti_3SiC_2:TiC, 84:16, matrix gave similar results to a pure Ti_3SiC_2 matrix, future work would benefit from a more pure matrix.
- This work successfully completed creep testing on three specimens; two on the monolithic samples and one of the SiC fiber-reinforced samples. Future work is recommended to complete more tests to ensure reproducibility of data. In addition

to testing needed at 1100 °C and 20 MPa, more testing is recommended to explore the 1000-1200 °C temperature range and up to 100 MPa for further comparison with Radovic et al.[66, 90]

- Studies on the fracture toughness are also recommended for further comparison with the work of others.

REFERENCES

1. Spencer, C.B., Cordoba, J., Sakulich, A., Obando, N., Radovic, M., Oden, M., Hultman, L., and Barsoum, M.W., *On the Reactivities of Ti_2AlC and Ti_3SiC_2 with SiC Fibers and Powders up to Temperatures of 1550°C.* Submitted to J. of Amer. Cer. Soc, 2010.

2. Spencer, C.B., Cordoba, J.M., Sakulich, A., Obando, N., Radovic, M., Oden, M., Hultman, L., and Barsoum, M.W., *Processing of Ti_2AlC Matrix Composites Reinforced with Al_2O_3 Fibers.* Submitted to: J. Amer. Cer. Soc., 2010.

3. Peters, S.T., ed. *Handbook of Composites*. 1998, Chapman & Hall: London.

4. Kragnes, E.D., *Processing and mechanical behavior of tape cast and laminated silicon cabide whisker/alumina composites*. 1988, Pennsylvania State University: Happy Valley.

5. Holtz, A.R., and Grether, M.F., *High temperature properties of three Nextel ceramic fibers,* in *32nd International SAMPE Symposium and Exhibition* 1987: Anaheim Convention Center.

6. Newkirk, M.S., Urquart, A.W., Zwicker, H.R., and Brevel, E., *Formation of LANXIDE™ ceramic composite material.* J. Mater. Res., 1986. 1(1): p. 81-88.

7. Stinton, D.P., Besmann, T.M., and Louden, R.A., *Advanced ceramics by chemical vapor deposition techniques.* Am. Ceram. Soc. Bull., 1988. 67(2): p. 350-355.

8. Jones, R.M., *Mechanics of Composite Materials*. 2nd ed. 1999, Philadelphia: Taylor & Francis, Inc. 519.

9. Mazdiyasni, K.S., ed. *Fiber Reinforced Ceramic Composites: Materials, Processing and Technology*. 1990, Noyes Publications: New Jersey.

10. Barsoum, M.W., and El-Raghy, T., *The MAX Phases: Unique New Carbide and Nitride Materials.* American Scientist, 2001. 89(July-August): p. 334-343.

11. Jeitschko, W., Nowotny, H., and Benesovsky, F., *Kohlenstoffhaltige ternare Verbindungen (H-Phase).* Monatsh. Chem., 1963. 94: p. 672-676.

12. Jeitschko, W., Nowotny, H., and Benesovsky, F., *Ti_2AlN, eine stickstoffhaltige H-Phase.* Monatsh. Chem., 1963. 94: p. 1198-1200.

13. Jeitschko, W., Nowotny, H., and Benesovsky, F., *Carbides of Formula Ti_2MC.* Journal of the Less-Common Metals, 1964(7): p. 133-138.

14. Barsoum, M.W., *Physical propeties of the MAX phases*, in *Encyclopedia of Materials: Science and Technology*, C. Buschow, Flemings, Kramer, Mahajan, and Veyssiere, Editor. 2001, Elsevier Ltd. p. 1-11.

15. Nowotny, H., *Struktuchemie Einiger Verbindungen der Ubergangsmetalle mit den elementen C, Si, Ge, Sn.* Prog. Solid St. Chem., 1970. 2.

16. Goto, T., and Harai, T., *Chemically Vapor Deposited Ti_3SiC_2.* Mater. Res. Bull., 1987. 22: p. 1195-1202.

17. Dubois, S., Cabioc'h, T., Chartier, P., Gauthier, V., and Jaouen, M., *A New Ternary Nanolaminate Carbide: Ti_3SnC_2.* J. Am. Ceram. Soc., 2007. 90.

18. Lin, Z., Zhou, M., Zhou, Y., Li, M., and Wang, J., *Microstructures and Theoretical Bulk Modulus of Layered Ternary Tantalum Aluminum Carbides.* J. Am. Ceram. Soc., 2006. 89.

19. Pietzka, M.A., and Schuster, J.C., *Summary of constitution data of the system Al-C-Ti.* J. Phase Equilibria, 1994. 15.

20. Wolfsgruber, H., Nowotny, H., and Benesovsky, F., *Die Kristallstruktur von Ti_3GeC_2.* Monatsh. Chem., 1967. 98.

21. Etzkorn, J., Ade, M., Kotzott, D., Kleczek, M., and Hillebrecht, H., *Ti_2GaC, Ti_4GaC_3, and Cr_2GaC--Synthesis, crystal growth and structure analysis of Ga-containing MAX-phases $M_{n+1}GaC_n$ with M=Ti, Cr and n=1,3.* J. Solid State Chem., 2009. 182.

22. Hogberg, H., Eklund, P., Emmerlich, J., Birch, J., and Hultman, L., *Epitaxial Ti_2GeC, Ti_3GeC_2, and Ti_4GeC_3 MAX-phase thin films grown by magnetron sputtering.* J. Mater. Res., 2004. 20.

23. Hu, C., Li, F., Zhang, J., Wang, J., Wang, J., and Zhou, Y., *Nb_4AlC_3.* Scripta Materialia, 2007. 57.

24. Hu, C., Zhang, J., Wang, J., Li, F., Wang, J., and Zhou, Y., *Crystal Structure of V_4AlC_3: A New Layered Ternary Carbide.* J. Am. Ceram. Soc., 2008. 91.

25. Palmquist, J.P., Li, S., Persson, P.O.A., Emmerlich, J., Wilhelmsson, O., Hogberg, H., Katnelson, M.I., Johansson, B., Eriksson, O., Hultman, L., and Jansson, U., *$M_{n+1}AX_n$ phases in the Ti-Si-C system studied by thin-film synthesis and ab initio calculations.* Physical Review B, 2004. 70.

26. Procopio, A.T., Barsoum, M.W., and El-Raghy, T., *Characterization of Ti_4AlN_3.* Metallurgical and Materials Transaactions A, 2000. 31A.

27. Rawn, C.J., Barsoum, M.W., El-Raghy, T., Procipio, A., Hoffmann, C.M., and Hubbard, C.R., *Structure of Ti_4AlN_3--a layered $M_{n+1}AX_n$ nitride.* Materials Research Bulletin, 2000. 35.

28. Zhou, Y., et al., *New MAX-Phase Compounds in the V-Cr-Al-C System.* J. Am. Ceram. Soc., 2008. 91(4): p. 1357-1360.

29. Barsoum, M.W., *The $M_{N+1}AX_N$ Phases: A New Class of Solids; Thermodynamically Stable Nanolaminates.* Prog. Solid St. Chem., 2000. 28: p. 201-281.

30. Jeitschko, W., and Nowotny, H., *Die Kristallstructur von Ti_3SiC_2 - Ein Neuer Komplxcarbid-Type.* Monatsh. Chem., 1967. 98: p. 329-337.

31. Zhou, Y.C., and Wang, X.H., *Deformation of polycrystalline Ti_2AlC under compression.* Mat Res Innovat, 2001. 5: p. 87-93.

32. Barsoum, M.W., Brodkin, D., and El-Raghy, T., *Layered Machinable Ceramics For High Temperature Applications.* Scripta Materialia, 1997. 36(5): p. 535-541.

33. Barsoum, M.W., Ali, M., and El-Raghy, T., *Processing and Characterization of Ti_2AlC, Ti_2AlN, and $Ti_2AlC_{0.5}N_{0.5}$.* Metallurgical and Materials Transactions A, 2000. 31A: p. 1857-1865.

34. Hettinger, J.D., Lofland, S.E., Finkel, P., Palma, J., Harnell, K., Gupta, S., Ganguly, A., El-Raghy, T., and Barsoum, M.W., *Electrical Transport, Thermal Transport and Elastic Properties of M_2AlC (M=Ti, Cr, Nb and V) Phases.* Phys. Rev. B, 2005. 72: p. 115-120.

35. Radovic, M., Ganguly, A., Barsoum, M.W., Zhen, T., Finkel, P., Kalidindi, S.R., and Lara-Curzio, E., *On the Elastic Properties and Mechanical Damping of Ti_3SiC_2, Ti_3GeC_2, $Ti_3Si_{0.5}Al_{0.5}C_2$ and Ti_2AlC in the 300-1573 K Temperature Range.* Acta Materialia, 2006. 54.

36. Manoun, B., Saxena, S.K., Barsoum, M.W., and El-Raghy, T., *High-Pressure Study of Ti_2AlN and Ti_2AlC.* J. Phys. Chem. Solids, 2006. 67: p. 2091.

37. Barsoum, M.W., Brodkin, D., and El-Raghy, T., *Layered Machinable Ceramics For High Temperature Applications.* Scripta Materialia 1996. 36(5): p. 535-541.

38. Wang, P., Mei, B., Hong, X., and Zhou, W., *Synthesis of Ti_2AlC by hot pressing and its mechanical and electrical properties.* Trans. Nonferrous Met. Soc. China, 2007. 17: p. 1001-1004.

39. Sundberg, M., Malmqvist, G., Magnusson, A., and El-Raghy, T., *Alumina forming high temperature silicides and carbides.* Ceramics International, 2004(30): p. 1899-1904.

40. Wang, X.H., and Zhou, Y.C., *High-Temperature Oxidation Behavior of Ti_2AlC in Air.* Oxidation of Metals, 2003. 59(3/4): p. 303-320.

41. Barsoum, M.W., Tzenov, N., Procopio, A., El-Raghy, T., and Ali, M., *Oxidation of $Ti_{n+1}AlX_n$ (n=1-3 and X=C, N) II. Experimental Results.* Journal of The Electrochemical Society, 2001. 148(8): p. C551-C562.

42. Barsoum, M.W., *Oxidation of $Ti_{n+1}AlX_n$ (n=1-3 and X=C, N): I. Model.* J. Electrochem. Soc., 2001. 148(8).

43. Byeon, J.W., Liu, J., Hopkins, M., Fischer, W., Garimella, N., Park, K.B., Brady, M.P., Radoviv, M., El-Raghy, T., and Sohn, Y.H., *Microstructure and Residual Stress of Alumina Scale Formed on Ti_2AlC at High Temperature in Air.* Oxidation of Metals, 2007(68): p. 97-111.

44. Barsoum, M.W., and El-Raghy, T., *Synthesis and Charaterization of a Remarkable Ceramic: Ti_3SiC_2.* J. Am. Ceram. Soc., 1996. 79.

45. Nickl, J.J., Schweitzer, K.K., and Luxenberg, P., *Gaphasenabscheidung im Systeme Ti-C-Si.* J. Less Common Metals, 1972. 26.

46. Racault, C., Langlais, F., and Naslain, R., *Solid-state synthesis and characterization of the ternary phase Ti_3SiC_2* J. Mater. Sci. , 1994. 29: p. 3384.

47. Emmerlich, J., Hogberg, H., Sasvari, S., Persson, P.O.A., Hultman, L., Palmquist, J.P., Jansson, U., Molina-Aldareguia, J.M., and Czigany, Z., *Growth of Ti_3SiC_2 thin films by elemental target magnetron sputtering.* J. Appl. Phys., 2004. 96(9): p. 4817.

48. Hogberg, H., Hultman, L., Emmerlich, J., Joelsson, T., Eklund, P., Molina-Aldareguia, J.M., Palmquist, J.P., Wilhelmsson, O., and Jansson, U., *Growth and characterization of MAX-phase thin films.* Surf. Coat. Tech., 2005. 193(1-3): p. 6.

49. Hu, J.J., Bultman, J.E., Patton, S., and Zabinski, J.S., *Pulsed Laser Deposition and Properties of $M_{n+1}AX_n$ Phase Formulated Ti_3SiC_2 Thin Films* Tribology Lett., 2004. 16(1/2): p. 113.

50. Lis, J., and Pampuch, R., *Reaction sintering phenomena of self-propagating high-temperature synthesis-derived ceramic powders in the Ti-Si-C system.* Solid State Ionics, 1997. 101-103(1-2): p. 59.

51. Riley, D.P., Kisi, E.H., and Phelan, D., *SHS of Ti_3SiC_2: ignition temperature depression by mechanical activation* J. Euro. Ceram. Soc. , 2006. 26(6): p. 1051.

52. Arunajatesan, S., and Carim, A.H., *Synthesis of Titanium Silicon Carbide.* J. Am. Ceram. Soc., 1995. 78(3): p. 667.

53. Zhang, Z.F., Sun, Z.M., and Hashimoto, H., *Rapid synthesis of ternary carbide Ti_3SiC_2 through pulse-discharge sintering from Ti/Si/TiC powders.* Metall. Mater. Trans. A, 2002. 33(11): p. 3321.

54. Zhang, Z.F., Sun, Z.M., Hashimoto, H., and Abe, T., *A new synthesis reaction of Ti_3SiC_2 through pulse discharge sintering Ti/SiC/TiC powder.* Script. Mater., 2001. 45(12): p. 1461.

55. Gao, N.F., Li, J.T., Zhang, D., and Miyamoto, Y., *Rapid synthesis of dense Ti_3SiC_2 by spark plasma sintering.* J. Eur. Cer. Soc., 2002. 22(13): p. 2365.

56. Tang, K., Wang, C.A., Wu, L.F., Guo, X.J., Xu, X.L., and Huang, Y., *Sintering of Ti_3SiC_2 with B_2O_3 additions* Ceram. Inter., 2002. 28(7): p. 761.

57. Li, J.F., Matsuki, T., and Watanabe, R., *Fabrication of highly dense Ti_3SiC_2 ceramics by pressureless sintering of mechanically alloyed elemental powders.* J. Mater. Sci. , 2003. 38(12): p. 2661-2666.

58. Li, J.F., Matsuki, T., and Watanabe, R., *Combustion Reaction During Mechanical Alloying Synthesis of Ti_3SiC_2 Ceramics from 3Ti/Si/2C Powder Mixture.* J. Am. Ceram. Soc., 2005. 88(5): p. 1318.

59. Li, S.B., and Zhai, H.X., *Synthesis and Reaction Mechanism of Ti_3SiC_2 by Mechanical Alloyinh of Elemental Ti, Si and C Powders.* J. Am. Ceram. Soc., 2005. 88(8): p. 2092-2098.

60. Li, S.B., Zhai, H.X., Zhou, Y., and Zhang, Z.L., *Synthesis of Ti_3SiC_2 powders by mechanically activated sintering of elemental powders of Ti, Si and C.* Mater. Sci. Eng. A, 2005. 407(1-2): p. 315.

61. Zhang, H.B., Bao, Y.W., and Zhou, Y.C., *Current Status in Layered Ternary Carbide Ti_3SiC_2, a Review.* J. Mater. Sci. Technol., 2009. 25.

62. El-Raghy, T., Barsoum, M.W., Zavaliangos, A., and Kalidindi, S.R., *Processing and Mechanical Properties of Ti_3SiC_2:II, Effect of Grain Size and Deformation Temperature.* J. Am. Ceram. Soc., 1999. 82(10): p. 2855-2860.

63. Barsoum, M.W., Ho-Duc, L.H., Radovic, M., and El-Raghy, T., *Long Time Oxidation of Ti_3SiC_2, Ti_3SiC_2/SiC and Ti_3SiC_2/TiC Composites in Air.* J. Electrochem. Soc., 2003. 150.

64. Sun, Z., Zhou, Y., and Li, M., *Cyclic-Oxidation Behavior of Ti_3SiC_2-Base Material at 1100 C.* Oxidation of Metals, 2002. 57.

65. Liu, G., Li, M., Zhang, Y., and Zhen, Y., *Cracking behavior of oxide scale formed on Ti_3SiC_2-based ceramic.* Materials Science and Engineering, 2003. A360.

66. Radovic, M., Barsoum, M.W., El-Raghy, T., and Wiederhorn, S.M., *Tensile creep of coarse-grained Ti_3SiC_2 in the 1000-1200 C temperature range.* Journal of Alloys and Compounds, 2003. 361: p. 299-312.

67. Zhen, T., Barsoum, M.W., Kalidindi, S.R., Radovic, M., Sun Z.M., and El-Raghy, T., *Compressive creep of fine and coarse-grained Ti_3SiC_2 in air in the 1100-1300 C temperature range.* Acta Materialia, 2005. 53.

68. Barsoum, M.W., *Fundamentals of Ceramics*. Second ed. Series in Materials Science and Engineering, ed. B. Cantor, and Goringe, M.J. 2003, New York: Taylor & Francis. 603.

69. Chen, J., Liu, M., Bao, Y., and Zhou, Y., *Failure-mode dependence of the strengthening effect in Ti_3AlC_2/10 vol.% Al_2O_3 composite.* Int. J. Mat. Res., 2006. 97(8): p. 1115-1118.

70. Benko, E., Klimczyk, P., Mackiewciz, S., Barr, T.L., and Piskorska, E., *cBN-Ti_3SiC_2 composites.* Diamond and Related Mater., 2004. 13(3): p. 521.

71. Wang, L.J., Jiang, W., Chen, L.D., and Bai, G.Z., *Microstructure of Ti_5Si_3/TiC/Ti_3SiC_2 and Ti_5Si_3/TiC nanocomposites in situ synthesized by spark plasma sintering* J. Mater. Res., 2004. 19(10): p. 3004.

72. Konoplyuk, S., Abe, T., Uchimoto, T., and Takagi, T., *Synthesis of TiSiC/TiC composites from TiH/SiC/TiC powders.* Mater. Lett., 2005. 59(18): p. 2342.

73. Konoplyuk, S., Abe, T., Uchimoto, T., and Takagi, T., *Ti_3SiC_2/TiC composites prepared by PDS.* J. Mater. Sci., 2005. 40(13): p. 3409.

74. Ho-Duc, L.H., El-Raghy, T., and Barsoum, M.W., *Synthesis and characterization of 0.3 Vf TiC-Ti_3SiC_2 and 0.3 Vf SiC-Ti_3SiC_2 composites.* Journal of Alloys and Compounds, 2003. 350: p. 303-312.

75. Gupta, S., Filimonov, D., Palanisamy, T., El-Raghy, T., and Barsoum, M.W., *Ta_2AlC and Cr_2AlC Ag-based composites - New solid lubricant materials for use over a wide temperature range against Ni-based superalloys and alumina.* Wear, 2007. 262: p. 1479-1489.

76. Amini, S., Ni, C., and Barsoum, M.W., *Processing, microstructural characterization and mechanical properties of a Ti_2AlC/nanocrystalline Mg-matrix composite.* Comp. Sci. and Tech., 2009. 69: p. 414-420.

77. Ashby, M.F., and Jones, D.R.H., *Engineering Materials 1: An Introduction to Properties, Applications and Design*. Third ed. 1980, Burlington: Elsevier Ltd. 424.

78. Barsoum, M.W., El-Raghy, T., Farber, L., Amer, M., Christini, R., and Adams, A., *The Topotaxial Transformation of Ti_3SiC_2 To Form a Partially Ordered Cubic $TiC_{0.67}$ Phase by the Diffusion of Si into Molten Cryolite.* J. Electrochem. Soc., 1999.

79. El-Raghy, T., and Barsoum, M.W., *Processing and mechanical properties of Ti_3SiC_2: part I: reaction path and microstructure evolution.* J. Am. Ceram. Soc., 1999. 82.

80. Ganguly, A., Zhen, T., and Barsoum, M.W., *Synthesis and Mechanical Properties of Ti_3GeC_2 and $Ti_3(Si_xGe_{1-x})C_2$ (x=0.5, 0.75) Solid Solutions.* J. Alloys and Cmpnds, 2004. 376.

81. Kisi, E.H., Wu, E., Zobec, J.S., Forrester, J.S., and Riley, D.P., *Inter-Conversion of $M_{n+1}AX_n$ Phases in the Ti-Al-C System.* J. Am. Ceram. Soc., 2007. 90.

82. Emmerlich, J., Hogberg, H., Eklund, L., Wilhelmsson, O., Jansson, U., Music, D., Schneider, J.M., and Hultman, L., *Thermal Stability of MAX-phase Ti_3SiC_2 Thin Films.* Acta Materialia, 2007. 55.

83. Farber, L., and Barsoum, M.W., *Isothermal Sections in the Cr-Ga-N System in the 650-1000 C Temperature Range.* J. Mater. Res., 1999. 14: p. 2560.

84. Du, Y., Schuster, J., Seifert, H., and Aldinger, F., *Experimental Investigation and Thermodynamic Calculation of the Titanium-Silicon-Carbon System.* J. Am. Ceram. Soc., 2000. 83: p. 197.

85. El-Raghy, T., Chakraborty, S., and Barsoum, M.W., *Synthesis and Characterization of Hf_2PbC, Zr_2PbC and M_2SnC (M=Ti, Hf, Nb and Zr).* J. Eur. Cer. Soc., 2000. 20.

86. El-Raghy, T., and Barsoum, M.W., *Diffusion Kinetics of the Carburization and Silicidation of Ti_3SiC_2.* J. Appl. Phys., 1998. 83: p. 112.

87. El-Raghy, T., Barsoum, M.W., and Sika, M., *Reaction of Al with Ti_3SiC_2 in the 800-1000 C Temperature Range.* Mater. Sci. Eng., 2001. 298: p. 174.

88. Wakelkamp, W.J.J., van Loo, F.J.J., and Metselaar, R., *Phase Relations in the Ti-Si-C System.* Journal of the European Ceramic Society, 1991. 8: p. 135-139.

89. Carroll, D.F., and Wiederhorn, S.M., *High Temperature Creep Testing of Ceramics.* Int. J. High Tech. Cer., 1988. 4: p. 227-241.

90. Radovic, M., Barsoum, M.W., El-Raghy, T., and Wiederhorn, S.M., *Tensile Creep of Fine Grained (3-5 um) Ti_3SiC_2 in the 1000-1200 C Temperature Range.* Acta Materialia, 2001. 49: p. 4103-4112.